



저작자표시-비영리-변경금지 2.0 대한민국

이용자는 아래의 조건을 따르는 경우에 한하여 자유롭게

- 이 저작물을 복제, 배포, 전송, 전시, 공연 및 방송할 수 있습니다.

다음과 같은 조건을 따라야 합니다:



저작자표시. 귀하는 원 저작자를 표시하여야 합니다.



비영리. 귀하는 이 저작물을 영리 목적으로 이용할 수 없습니다.



변경금지. 귀하는 이 저작물을 개작, 변형 또는 가공할 수 없습니다.

- 귀하는, 이 저작물의 재이용이나 배포의 경우, 이 저작물에 적용된 이용허락조건을 명확하게 나타내어야 합니다.
- 저작권자로부터 별도의 허가를 받으면 이러한 조건들은 적용되지 않습니다.

저작권법에 따른 이용자의 권리와 책임은 위의 내용에 의하여 영향을 받지 않습니다.

이것은 [이용허락규약\(Legal Code\)](#)을 이해하기 쉽게 요약한 것입니다.

[Disclaimer](#)



Ph.D. DISSERTATION

Design of Multicomponent Metal Alloy Electrocatalysts for Improving Electrochemical Performance

고효율 촉매전극을 위한 다원계 금속 합금 전기

촉매 연구

By

Hoonkee Park

February 2020

**DEPARTMENT OF MATERIALS SCIENCE AND
ENGINEERING COLLEGE OF ENGINEERING SEOUL
NATIONAL UNIVERSITY**

Design of Multicomponent Metal Alloy Electrocatalysts for Improving Electrochemical Performance

Advisor: Prof. Ho Won Jang

By
Hoonkee Park

**A thesis submitted to the Graduate Faculty of Seoul National University
in partial fulfillment of the requirements
for the Degree of Doctor of Philosophy
Department of Materials Science and Engineering**

December 2019

Approved

by

Chairman of Advisory Committee: Yong-Chang Joo

Vice-Advisory Committee: Ho Won Jang

Advisory Committee: Jin Young Kim

Advisory Committee: Kim Dong Wan

Advisory Committee: Sang Hyun Ahn

Abstract

Widespread application of electrochemical water splitting for energy conversion is largely dependent on the progress in developing not only efficient but also cheap and scalable electrocatalysts. Transition metal based metal oxides/hydroxide, alloys which can be synthesized with scalable technique such as electrochemical deposition are promising candidate for efficient electrocatalysts. Among the various metal candidates, Ni-based metal oxide/hydroxide, metal alloys have become a hot topic for electrochemical hydrogen generation by water oxidation. However, the actual conversion efficiency achieved with Ni-based electrocatalysts is considerably less than the noble metal based electrocatalysts because of drawbacks such as relatively low stability and slow kinetics of oxygen evolution reaction. In this respect, diverse engineering strategies such as formation of nanostructured surface, control of grain boundary composition, and development of electrocatalyst with new composition are considered to have a marked effect in terms of improving the overall efficiency of hydrogen generation.

This thesis proposes the breakthroughs to overcome aforementioned limitations of non-noble metal based electrocatalysts. There are three major

strategies were conducted to accomplish high efficiency near or over the precious metal based electrocatalysts for practical issue.

The first study reports the correlation between surface grain boundary density and water splitting efficiency based on single FCC phase binary NiFe alloy synthesized by arc-melting and electrodeposition. Among various metal alloys, NiFe alloy is the promising electrocatalysts to replace noble metal in terms of oxygen evolution reaction. And this study revealed that the oxygen evolution reaction activity of bare NiFe alloys can be changed drastically by controlling the surface grain boundary density. Under the extremely increased grain boundary density, a NiFe alloy electrocatalysts can lead to a low overpotential for current density 10 mA/cm² (300mV) and extremely high electrochemical surface area (ECSA) than micrometer-size grain NiFe alloy without additional catalyst. Electron backscatter diffraction and X-ray diffraction shows that single FCC phase NiFe alloy are successively synthesized by arc-melting and electrodeposition. This systematic study provides a viewpoint on the crucial role of the grain boundary on activity of oxygen evolution reaction, and the proposed concept is applicable to various metal alloy systems.

The second study handles the overall water splitting and hydrogen production efficiency using NiFe (oxy)hydroxide and NiMo alloy as water

splitting electrocatalysts, followed by the PV-EC system assisted by perovskite/Si tandem solar cell. Using facile and low cost synthesis, anodization and electrodeposition, electrocatalysts are properly synthesized to maximize the surface area and stability. High-performance perovskite/Si tandem cell attributed to extremely increase the operating current density of the combined system achieve a value of 14.24 mA/cm^2 , $\eta_F = 100\%$ and $J_{sc} = 14.2 \text{ mA/cm}^2$, the solar-to-hydrogen (STH) efficiency was determined to be 17.52%. The appropriate combination of oxygen evolution catalysts, hydrogen evolution catalysts and solar cells for PV-EC system enable to break new ground for development of low-cost, highly efficient hydrogen generation devices.

The third is introduction of medium entropy alloys (MEAs) to enhance stability and electrochemical efficiency and surface reaction kinetics by controlling the composition. The synergistic effect of newly explored quartenary metal alloys determine overall properties of electrochemical water splitting. While high entropy alloys (HEAs) has attracted intension as stable at harsh environment and potential of cocktail effect, its crucial role in water splitting efficiency has not yet been fully understood. This study firstly compare the electrochemical properties of HEAs and MEAs, find the superb MEAs consist of Fe, Ni, Co, and Cr. Further catalyst synthesizing

process like anodization and CV activation achieve a remarkably reduced overpotential for current density of 10 mA/cm^2 , from 475 mV to 184 mV. Improved electrochemical activity is closely related to the increased surface area originate from anodization and substantial shifts in chemical oxidation that derive from the CV activation process. Proposed concept has considerable potential to explore new efficient water splitting electrocatalysts. Combined spectroscopic analysis and electrochemical study can reveal the clear relationship between the surface chemical oxidation derived from CV activation and oxygen evolution properties for water oxidation.

In this thesis, diverse approaches such as nanostructure, grain size control, oxygen evolution catalyst and medium entropy alloys are covered to make breakthrough for transition metal based electrochemical water splitting. This systematic study provides general strategy for enabling new active non-noble metal electrocatalyst and is applicable to overall hydrogen generation system.

Keyword: Metal hydroxide, Electrochemical water splitting, NiFe, Medium Entropy Alloy, Nanostructure, Electrocatalyst, Electrodeposition

Student Number: 2013-22476

Table of Contents

Abstract	1
Table of Contents	5
List of Tables	6
List of Figures	8
Chapter 1	13
Electrochemical water splitting: Basic principles	13
1.1 Introduction	14
1-2. Electrolysis Water Splitting System	17
1-3. Scope and objectives of the thesis	21
1-4. Reference	24
Chapter 2	25
Grain boundary as a dominant active sites for oxygen evolution reaction in metal alloy electrocatalysts	25
2-1. Introduction	26
2-2. Experimental method and characterization	28
2-3. Results and discussion	34
2-4. Conclusion	44

2-5. References.....	46
Chapter 3	50
Solution processed electrocatalysts with nanometer scale grain using earth abundant elements for overall water splitting reaction.....	50
 3-1. Introduction	51
 3-2. Experimental method and characterization.....	57
 3-3. Results and discussion	64
 3-4. Conclusion	82
 3-5. References.....	83
Chapter 4.....	92
 4-1. Introduction	93
 4-2. Experimental method and characterization.....	95
 4-3. Results and discussion	97
 4-4. Conclusion	104
 4-5. References.....	106
6. Summary	109
Abstract (in Korean).....	111

List of Tables

Table 3-1 Comparison between our results and various PV-EC systems that have been reported elsewhere.

List of Figures

Figure 1-1 Sustainable paths to produce hydrogen from renewable energy.

Figure 1-2 Oxygen and hydrogen evolution reaction (OER and HER) for overall water splitting.

Figure 1-3. Various strategies to enhance water splitting activities of non-noble metal based electrocatalysts.

Figure 2-1 Schematic illustration of fabrication process for various grain size NiFe binary alloy.

Figure 2-2 Schematic illustration of electrodeposition process for nanometer scale grain size NiFe binary alloy.

Figure 2-3 Schematic illustration of SPECM for in-situ observation of water splitting at NiFe binary alloy surface.

Figure 2-4 (a), (b) is the high resolution TEM images of 20 μm grain and 440 μm grain, respectively. (c) is X-ray diffraction patterns of different samples. (d), (e) show the EBSD images of 20 μm grain and 440 μm grain.

Figure 2-5 (a) Linear sweep voltammograms measured in 1 M NaOH at a scan rate of 10 mV/s for micrometer scale grain sized NiFe binary alloys. (b)

EIS measurement of micrometer scale grain sized NiFe binary alloy at 1.5V vs. RHE.

Figure 2-6 (a) Linear sweep voltammograms measured in 1 M NaOH at a scan rate of 10 mV/s for all samples. (b) EIS measurement of NiFe binary alloy at 1.5V vs. RHE for all samples.

Figure 2-7 Tafel plot of various grain sized NiFe binary alloys.

Figure 2-8 Charge transfer steps of typical metal hydroxide.

Figure 2-9 Electrochemical surface area measurement using double layer capacitance.

Figure 2-10 SPECM measurement of 440 μm grain and nanometer scale grain NiFe binary alloys.

Figure 3-1 Sketch diagram of electroforming process to make an NiFe alloy foil. Cathode electrode was rolling with continuous supplied bath solution, NiFe alloy foil are deposited on the other side of electrode coil.

Figure 3-2 Illustrated sketch of our synthesis procedure for forming a water splitting cell. The cathode material was deposited onto the NiFe alloy by using an electrodeposition method, and the anode material was obtained simply by anodizing the NiFe alloy. The key idea of our method is the direct

anodization of the metal alloy substrate for the synthesis of more efficient electrodes with long-term stability.

Figure 3-3 Structural characterization of the NiFe alloy, NiFe (oxy)hydroxide films and Ni₄Mo films on the NiFe alloy. (a), (b), (c) 3-dimensional atomic force spectroscopy images of bare NiFe alloy, NiFe (oxy)hydroxide films, and Ni₄Mo films. (d), (e), (f) SEM images of bare NiFe alloy, NiFe (oxy)hydroxide films, and Ni₄Mo films, respectively. The high-resolution TEM images of (g) NiFe (oxy)hydroxide and (h) Ni₄Mo film. The SAED patterns for the synthesized films are displayed in the insets of (g), (h).

Figure 3-4 XRD characteristics of the NiFe (oxy)hydroxide films and electrodeposited NiMo films.

Figure 3-5 Electrochemical performance of different catalyst electrodes as characterized by linear sweep voltammetry in 1 M NaOH aqueous electrolyte. (a) OER characteristics of different catalyst electrodes in a three-electrode configuration scanned in the direction from the positive to the negative potential on the RHE scale. (b) Tafel slopes for the OER electrode and (c) HER characteristics for the different catalyst electrodes in a three-electrode configuration scanned in the direction from the negative to

the positive potential. (d) Tafel slopes for the HER electrode. All scan rates were 1 mV s^{-1} .

Figure 3-6 2 electrode water splitting properties combining with a conventional 1.5 V battery. (a) Current density and (b) NiFe (oxy)hydroxide/NiMo water splitting system driven by an $\sim 1.5 \text{ V}$ AAA battery.

Figure 3-7 Chemical characterization of the NiFe (oxy)hydroxide and Ni_4Mo electrocatalysts. (a) and (b) XPS spectra for Fe and Ni before and after anodization. (c) Raman spectra for the bare NiFe alloy and NiFe (oxy)hydroxide films, (f) FT-IR spectra for the bare NiFe alloy and NiFe (oxy)hydroxide films. (d) and (e) the Ni and Mo XPS spectra for the Ni_4Mo films.

Figure 3-8 Combination of the silicon tandem cell with NiFe (oxy)hydroxide/NiMo electrodes for water splitting. (a) Overall water splitting characteristics versus Ni foam in a two-electrode configuration scanned from 2.0 V to 1.0 V. (b) Faradaic efficiency of the water splitting electrode. (c) Schematic diagram of the water splitting device. (d) $J-V$ curves for the silicon tandem cell and the NiFe LDH/NiMo electrodes in a two-electrode configuration under AM 1.5G 100 mW cm^{-2} illumination.

The aperture size of the tandem cell was 0.1875 cm^2 , and the catalyst electrode areas were $\sim 2\text{ cm}^2$ each. (e) Current density–time curve of the integrated water splitting device without external bias under chopped simulated AM 1.5G 100 mW cm^{-2} illumination.

Figure 4-1 Schematic illustration of conventional alloy and medium entropy alloy.

Figure 4-2 EBSD images of fabricated HEA and MEAs.

Figure 4-3 X-ray diffraction patterns of HEA and MEAs.

Figure 4-4 Hydrogen evolution reaction of HEA and MEAs.

Figure 4-5 Oxygen evolution reaction of HEA and MEAs.

Figure 4-6 Oxygen evolution reaction of $\text{Fe}_{60}(\text{CoNi})_{30}\text{Cr}_{10}$ MEAs after anodization and CV activation

Figure 4-7 SEM and TEM images of (a) Bare $\text{Fe}_{60}(\text{CoNi})_{30}\text{Cr}_{10}$ MEAs, (b) anodized MEAs, and (c) CV activated MEAs after anodization.

Chapter 1

Electrochemical water splitting: Basic principles

1.1 Introduction

In every aspect of our lives, we intensively use the fossil fuels and chemicals, which have limited amount of reserves. With the rapidly growing industry and population, the indiscriminate use of energy and materials only lead to the threat of a dearth of supply and rising costs. For instance, energy consumption is expected to rise by 56 % worldwide by 2040 with close to 80 % provided by fossil fuels.^[1-3] Considering that the population and industrial requirement is continuously increased, we should find a wise solution in this trend to maintain the sustainable development. The possible solution that we overcome current crisis is convert infinite resource into useful energy, like from solar energy to electricity, to maintain a balance between production and consumption.

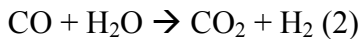
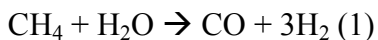
1-1-1. Sustainable and Future energy sources

The depletion of conventional fossil fuels and increasing energy crisis requires the development of newly and sustainable energy sources. Thus, it is extremely urgent to search viable alternative renewable energy to replace fossil fuel. Renewable energy sources include solar, wind, wave and biomass, in which solar energy possesses a theoretical potential of 1.2×10^5

TW, for more than other form of energy sources. Therefore, it can easily meet the world's total energy consumption. However, solar energy has two serious disadvantages, i.e., low-energy density, fluctuations with weather and hard to store for fairly long periods of time and distribute over long distances; therefore, technologies for the direct utilization of solar energy have been very limited.^[2]

1-1-2. From solar to hydrogen

Since the solar electricity produced by photovoltaics is still very expensive and, the efficient and inexpensive conversion of solar energy into chemical energy such as hydrogen energy has been considered to be a highly desirable way to satisfy long-term energy needs and cost-effectiveness, as shown in Figure 1-1. Currently, the dominant hydrogen production method is a steam reforming, which uses fossil fuel and emits large amount of carbon dioxide.



Hydrogen has to be produced from water using natural energies such as sunlight if one thinks of energy and environmental issues. Therefore,

achievement of solar hydrogen production from water has been urged. Some of carbon free hydrogen production methods are: (1) thermochemical water splitting which is mainly use nuclear energy, Figure 1-1. Some representative methods and energy source for hydrogen production. (2) Electrolysis water splitting, that use electricity from hydropower, wind and solar energy, (3) Photobiological and photoelectrochemical water splitting which use solar energy to split water into its constituent atom, hydrogen and oxygen. Among these carbon free hydrogen production methods the electrolysis water splitting assisted with solar cell is considered as one of the potential future eco-friendly rout that could enable the production of hydrogen using water as reactant and solar energy as primary energy source.^[4]

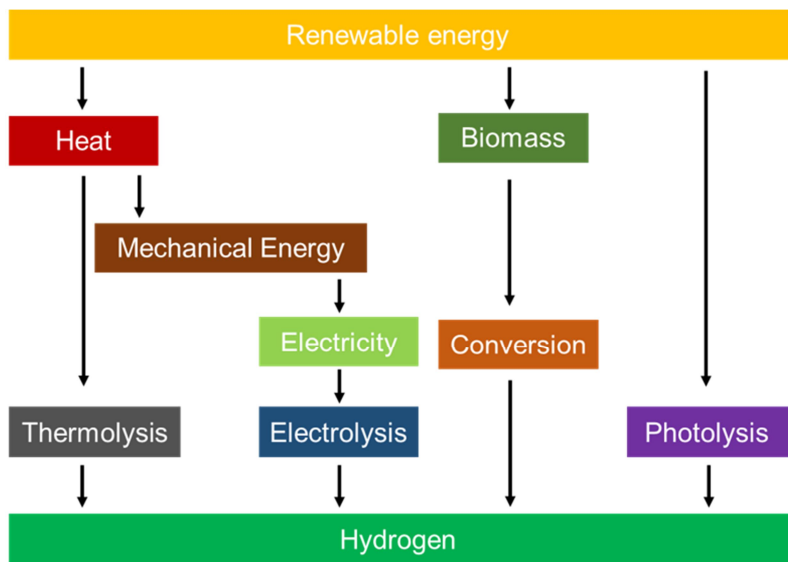
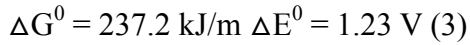
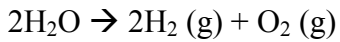


Figure 1-1 Sustainable paths to produce hydrogen from renewable energy.

1-2. Electrolysis Water Splitting System

The free energy change for the conversion of one molecule of H_2O to H_2 and $1/2 \text{ O}_2$ under standard conditions is $\Delta G = 237.2 \text{ kJ/mol}$, which corresponds to $\Delta E^\circ = 1.23 \text{ eV}$ per electron transfer according to the Nernst equation. This process must generate two electron-hole pairs per molecule of H_2 ($2 \times 1.23 \text{ eV} = 2.46 \text{ eV}$) or four electron-hole pairs per molecule of O_2 ($4 \times 1.23 \text{ eV} = 4.92 \text{ eV}$). ^[5] The overall water splitting reaction is composed of two half-reaction, the HER and OER. Thermodynamically, the water splitting reaction is an uphill reaction because of a large positive change in Gibbs free energy ($\Delta G = 237.2 \text{ kJ/mol}$). It is also known that the OER is an

essential component of light-driven water splitting systems, which provides protons and electrons for the production of hydrogen. The overall water splitting reaction in alkaline electrolyte is as follow.



Two water molecules dissociate and hydrogen arises at the cathode by this reaction. At the anode, oxygen arises and a water molecule is generated at the same time. As a result, when a water molecule dissociates, another water molecule moves to the anode. The liquid electrolyte allows ions to be transported between the electrodes and is not consumed in the chemical reaction, but is periodically replenished depending on the losses in the system. The electron-transfer processes at electrocatalyst/electrolyte junctions produce losses due to the concentration and kinetic overpotential needed to drive the HER and the OER. The energy required for electrolysis is therefore conventionally compared at overpotential for achieve current density of 10 mA/cm^2 to account for these losses.

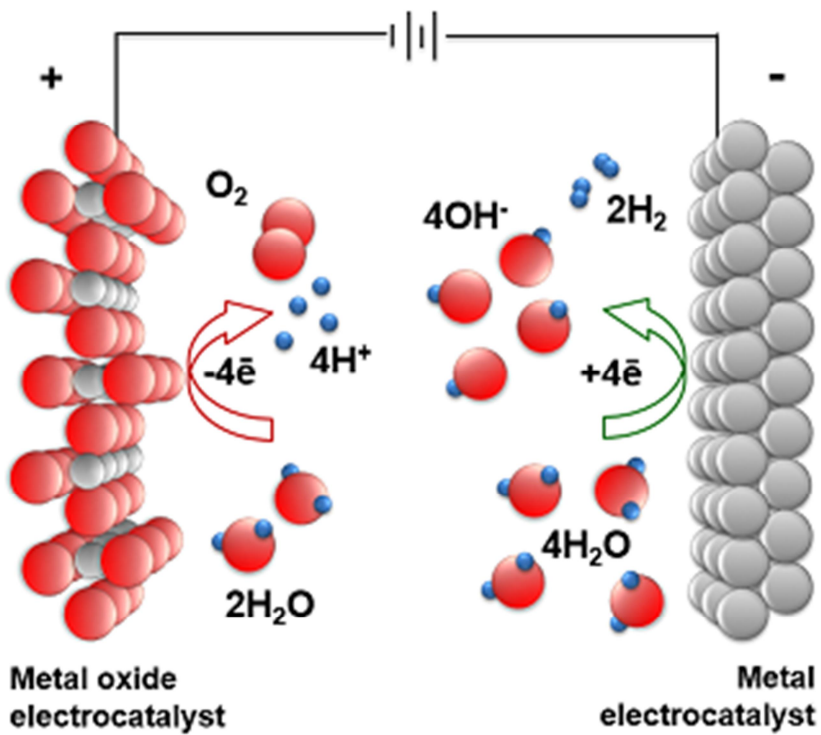


Figure 1-2 Oxygen and hydrogen evolution reaction (OER and HER) for overall water splitting.

1-2-2. Efficiencies for PEC water splitting cells

Electrochemical activity for water splitting can be directly evaluated by the hydrogen and oxygen evolution rate and current density, respectively. For PV-EC system, the applied potential and intensity of incident light should also be provided when performing an evaluation of activity. Thus,

three primary measures of efficiency are used, as follows. [3,5,7]

- Benchmark efficiency (suitable for mainstream reporting of stand-alone water splitting capability)
 - Solar-to-hydrogen conversion efficiency (STH)
- Diagnostic efficiencies (to characterize and understand materials system/interface performance)
 - Tafel slope
 - Overpotential

1-2-2-1. Solar-to-hydrogen conversion efficiency (STH)

STH efficiency is the most overarching of all efficiency metrics as it describes the overall efficiency of a PV-EC system exposed to broadband solar irradiance (e.g., Air Mass 1.5 Global illumination, 100 mW/cm²) under zero-bias conditions. Zero-bias means that there is no applied voltage between the working electrode and counter electrode, and all of the energy in the water splitting process is being supplied by sunlight. For standard STH efficiency can be expressed as chemical energy of the hydrogen produced divided by solar energy input from sunlight incident on the process. The chemical energy of the hydrogen produced can be calculated

from the rate of hydrogen production (mmol H₂/s) multiplied by the change in Gibbs free energy per mole of H₂ ($\Delta G^0 = 237 \text{ kJ/mol}$, 25 °C).^[7] In the denominator of the STH definition, the solar energy input from sunlight is incident illumination power density (P_{total}, in units of mW/cm²) multiplied by the illuminated electrode area (cm²).

$$\text{STH} = \left[\frac{I_{sc} (\text{mA}) * 1.23 (\text{V}) * n_F}{P_{\text{total}} \left(\frac{\text{mW}}{\text{cm}^2} \right) * \text{Area} (\text{cm}^2)} \right]_{\text{AM } 1.5G}$$

1-3. Scope and objectives of the thesis

This thesis focuses on the develop technology for fabricating highly efficient solar to fuel system using the nanostructured non-noble metal based electrocatalysts. Hydrogen is considered as an ideal energy carrier to meet these challenges since it is clean, renewable, carbon-free, and has a high energy density. Electrochemical assisted by photovoltaic (PV-EC) hydrogen production system is thus considered as a key technology of the future, attracting widespread attention. Among the commonly used transition metal based electrocatalysts, Ni based oxide/hydroxide attract a lot of attention due to their outstanding chemical stability, low cost, high efficient similar to that of noble metal. The rich diversity of metal oxides

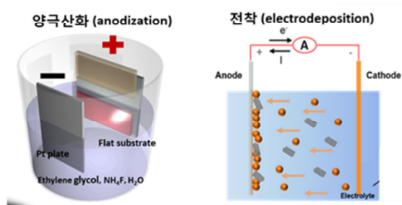
with multi-functions offers a lot of opportunities to develop high performance electrochemical water splitting. Even though metal oxides are promising candidate for electrochemical water splitting, they have their intrinsic limitations such as sluggish carrier transport, extraction and large electrical resistivity, and thus it is detrimental to electrochemical performance. Therefore, a variety of strategies have been introduced to address the aforementioned drawbacks of non-noble metal based electrocatalysts as water splitting electrodes for overall water splitting. Most of all, the anodic reaction will most likely involve oxidation of water. Due to the slow kinetics involving multi-electron and multi-proton transfers, water oxidation is particularly demanding and requires high overpotential. Thus, in this thesis, developing an efficient and practical anode system that can oxidize water to oxygen in a stable manner is introduced for the successful construction of high performance, commercially viable electrochemical cell.

Figure 1-6 shows suggesting ideas to improve PEC performance of metal oxides and final goal to approach practical field. The research presented in this thesis involves several engineering concept such as explore new composition, nanostructures, and PV-EC systems to access efficient hydrogen production efficiency and further expands the understanding and applicability of metal oxide anode for electrochemical water splitting system.

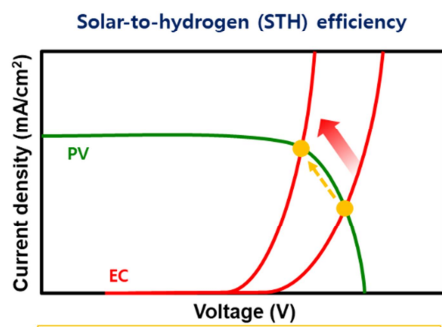
1. Optimal composition



2. Surface modification



3. Hydrogen generation (PV-EC system)



$$STH = \left[\frac{I_{sc}(\text{mA}) \times 1.23(\text{V}) \times \eta_F}{A_{\text{module}}(\text{cm}^2) \times P_{in}(\text{mW cm}^{-2})} \right]_{AM1.5G}$$

I_{sc} : Short-circuit current of the PV-EC

η_F : Faradaic efficiency

1.23 V : Reversible voltage of the water electrolysis

A_{module} : Area of the PV module

P_{in} : Power density of the incident light

Figure 1-3 Various strategies to enhance water splitting activities of non-noble metal based electrocatalysts.

1-4. Reference

- [1] A. E. Outlook, *US Department of Energy, United States Government Printing Office: Washington, DC, 2013.*
- [2] D. Kim, K. K. Sakimoto, D. Hong and P. Yang, *Angew. Chem. Int. Ed.*, **2015**, 54, 3259.
- [3] C. Jiang, S. J. Moniz, A. Wang, T. Zhang and J. Tang, *Chem. Soc. Rev.*, **2017**, 46, 4645.
- [4] H. L. Tuller, *Materials for renewable and sustainable energy*, **2017**, 6, 3.
- [5] M. G. Walter, E. L. Warren, J. R. McKone, S. W. Boettcher, Q. Mi, E. A. Santori and N. S. Lewis, *Chem. Rev.*, **2010**, 110, 6446.
- [6] H. M. Chen, C. K. Chen, R.-S. Liu, L. Zhang, J. Zhang and D. P. Wilkinson, *Chem. Soc. Rev.*, **2012**, 41, 5654.

Chapter 2

Grain boundary as a dominant active sites for oxygen evolution reaction in metal alloy electrocatalysts

2-1. Introduction

With the rapid increase of global temperature and depletion of fossil fuels, developing sustainable energy resources is crucial nowadays. Among the various renewable energy source generation approaches, water splitting has attracted increasing attention for clean energy generation and efficient energy storage. Electrochemical production of hydrogen from solar electricity is also an attractive option for generating energy in the form of hydrogen which could be used for electricity. Amidst many hydrogen generation techniques such as coal, wind, solar, and electrolysis, water splitting is a promising candidate that is environmentally friendly and highly efficient. However, it still remains a great challenge to develop sufficiently efficient electrocatalysts to generate hydrogen energy that is competitive with fossil fuels. Grain boundary could supply additional active sites that has potential to enhance overall water splitting properties in terms of overpotential and current density. This work may provide a cost-effective and simple way to develop the highly efficient hydrogen generation technique by control the surface grain boundary density.

2-1-1. Advantages of grain boundary at CO₂ reduction reaction

Grain boundary (GB) has a high potential to increase the activity of the materials, so it has attracted attention in many study. Especially in CO₂ reduction reaction, grain boundary is promising era because it can extremely enhance the CO₂ reduction efficiency with equal CO₂ reduction catalysts. As reported in many articles, the grain boundary of materials at surface has strong CO binding sites than the sites on terraces or stepped surfaces. As a results, the grain boundary could alter the reaction step, especially the CO dimerization step. Similar to the contribution on CO₂ reduction reaction, the grain boundary also could enhance the water splitting properties, as properly controlled. In this regard, various grain-sized NiFe binary alloys with single FCC phase, from nanometer scale to 440 micrometer scale, are evaluated to reveal the correlation of grain boundary density and electrochemical water splitting efficiency.

2-2. Experimental method and characterization

2-2-1. Arc-melting synthesis of micrometer scale grain sized NiFe alloy for electrocatalysts

The samples were produced by arc melting method using metallurgical ingredients above 99.9% purity under Ti-gettered high-purity Argon atmosphere. The alloy button was re-melted more than five times to improve the compositional homogeneity. The NiFe binary alloys were then suction casted into a water-cooled copper mold with a rectangular cavity (= 12 mm width × 4 mm thickness × 50 mm length). The suction casted alloys were homogenized at 1050 °C for 24 h in an Ar atmosphere and eventually quenched in water. The homogenized samples underwent cold rolling to a total rolling reduction ratio of 70–85% followed by annealing above the recrystallization temperature in an Ar atmosphere followed by water quenching. Recrystallization annealing condition is 900 °C 3 min for 20 micrometer grain NiFe alloy and 1250 °C 24 h for 440 micrometer grain NiFe alloy, respectively. The bulk samples were mechanically ground into a

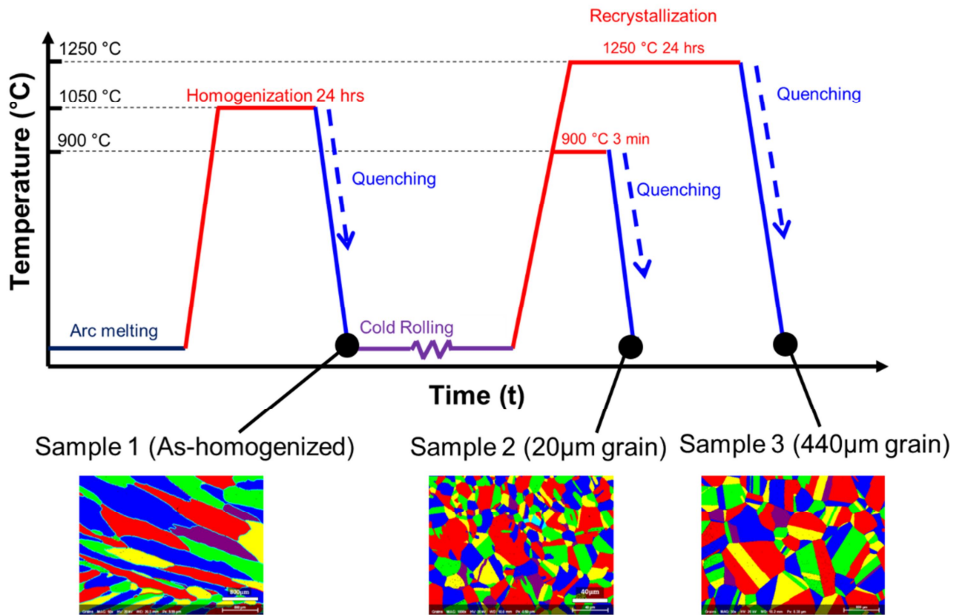


Figure 2-1 Schematic illustration of fabrication process for various grain size NiFe binary alloy.

15 μm -thick ribbon, with SiC abrasive paper down to P4000.

2-2-2. Pulsed electrodeposition for nanometer grain NiFe binary alloy

The electroforming of NiFe alloy was carried out in a three-electrode system with Ti foil (Alfa Aesar, annealed, 99.6%) as the working electrode, dimensionally stable anodes (DSA, Ti/IrO₂) as a counter electrode, and Ag/AgCl (3M) as the reference electrode, as shown in Figure 1. Ti foil was

cleaned with acetone, isopropyl alcohol, and distilled water by ultrasonication. The surface of the Ti foil was covered with adhesive tape, except for the active area ($1.5\text{ cm} \times 3.5\text{ cm}$). For the deposition of typical NiFe alloy, a Fe-Ni aqueous plating solution (400 ml) was prepared by dissolving 0.378 M (nickel sulfate hydrate ($\text{NiSO}_4 \cdot 6\text{H}_2\text{O}$, DAEJUNG), 0.122 M iron sulfate heptahydrate ($\text{FeSO}_4 \cdot 7\text{H}_2\text{O}$, DAEJUNG), 0.052 M boric acid (H_3BO_3 , JUNSEI) as a buffer reagent, 1.3 mM sodium saccharin dihydrate ($\text{C}_7\text{H}_4\text{NNaO}_3\text{S} \cdot 2\text{H}_2\text{O}$, DAEJUNG) as a stress reducer, and 0.082 M sodium chloride (NaCl , DAEJUNG) as a supporting reagent. To prevent the precipitation of iron species, 0.2 ml of hydrochloric acid (DAEJUNG) was added. For NiFe alloys with various compositions, the total amount of moles of Ni and Fe precursors were controlled to 0.5 M. Before electroforming, Ti foil was soaked for 5 min in diluted HCl to remove the residual oxide layer. The optimized current density of -40 mA/cm² vs Ag/AgCl was applied for the electroforming of NiFe alloy. After the electroforming, the prepared samples were rinsed with deionized water and dried by blowing nitrogen gas, and the adhesive tapes were detached and electrodeposited alloys were carefully peeled off from the Ti foil. Unlike previous methods, pulsed electrodeposition enables conformal deposition on the bottom electrode, which affects the electrochemical property.

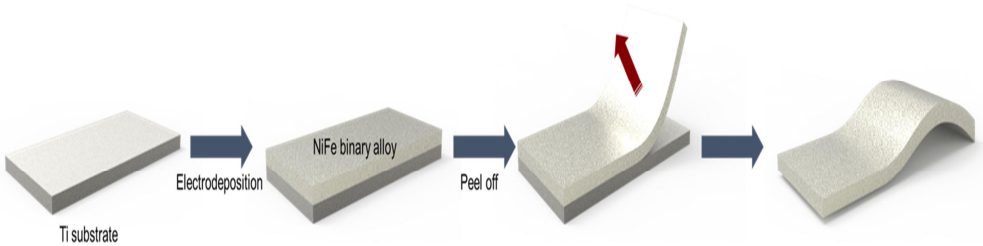


Figure 2-2 Schematic illustration of electrodeposition process for nanometer scale grain size NiFe binary alloy

2-2-3. Scanning Photoelectrochemical Microscopy (SPECM)

The direct observation of water splitting reaction at surface, especially grain boundary and grain, was conducted by scanning photoelectrochemical

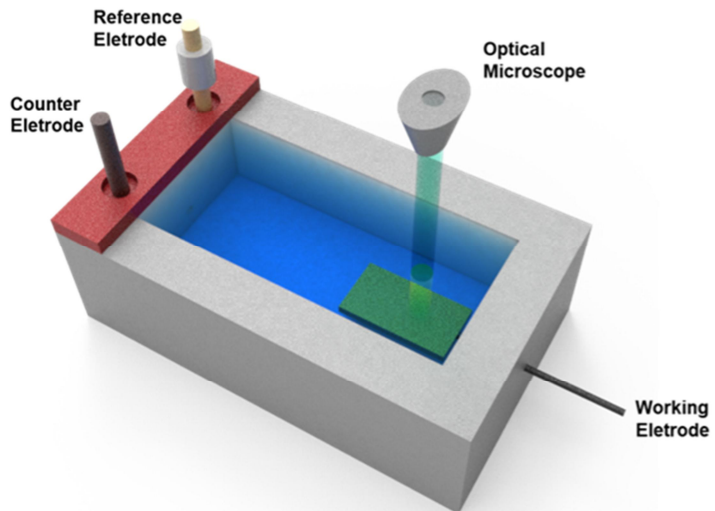


Figure 2-3 Schematic illustration of SPECM for in-situ observation of water splitting at NiFe binary alloy surface.

microscopy (SPECM).

2-2-4. Physical characterization

The morphologies of NiFe binary alloys were characterized by field emission scanning electron microscopy (MERLIN Compact, JEOL). Bright-field and high-resolution transmission electron microscopy (JEM-2100F, JEOL) with 200 kV field-emission images were obtained to investigate the microstructure of the NiFe alloys. X-ray diffraction (XRD) characterization was performed to confirm the crystalline phase of NiFe alloys. EBSD measurement was performed with a Hikari camera and the TSL OIM data-collection software. The EBSD scan step size was 75 nm and a tolerance angle of 5° was used for grain identification.

2-2-4. Electrochemical characterization

Electrochemical water splitting measurements (Ivium Technologies, Nstat) were performed with a three-electrode system using a 3 M Ag/AgCl reference electrode and a Pt wire as a counter electrode with 1 M NaOH electrolyte solution, with the pH of the electrolyte considered to be 14. All potentials were applied versus a 3 M Ag/AgCl reference electrode and converted into the reversible hydrogen electrode (RHE). The current was

recorded using a computer-controlled multichannel electrochemical analyzer potentiostat (IVIUM STAT), which was used to simultaneously control the potential. EIS spectra were recorded using the same potentiostat in the preceding three-electrode configuration. A sinusoidal voltage perturbation with an amplitude of 10 mV and frequencies ranging from 350 kHz to 1 Hz was superimposed onto the bias voltage to gather the EIS data. The EIS data were fit to the equivalent circuits. Electrochemical impedance spectroscopy (EIS) was conducted by applying 0.5 V vs. Ag/AgCl. The measured spectra were fitted by using the ZSimpWin software.

2-3. Results and discussion

2-3-1. Fabrication of micrometer grain-sized NiFe binary alloys using the arc-melting process

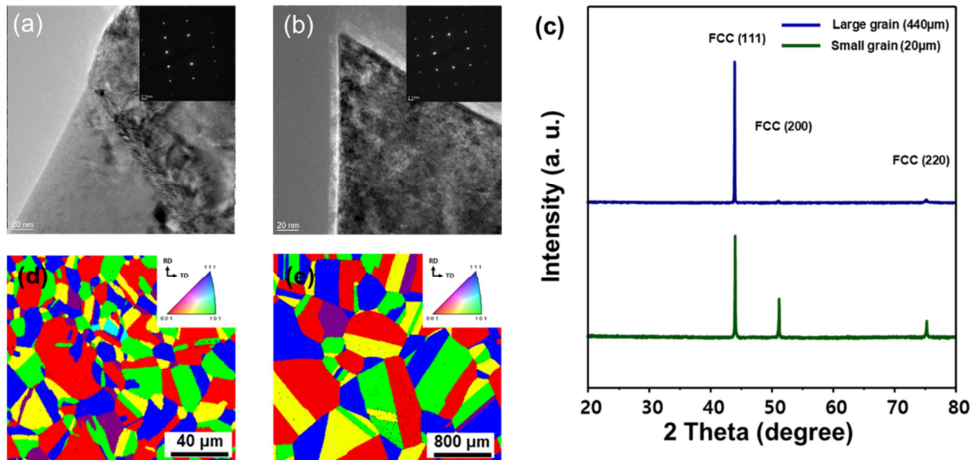


Figure 2-4 (a), (b) is the high resolution TEM images of 20 μm grain and 440 μm grain, respectively. (c) is X-ray diffraction patterns of different samples. (d), (e) show the EBSD images of 20 μm grain and 440 μm grain.

To fabricate NiFe binary alloys for intended phase and composition, the use of the arc-melting process has several advantages. Arc-melting fabrication enables the formation of precise atomic ratio between compositions and control of grain size assisted by changing recrystallization condition from the low temperature, short time to high temperature, long times. In addition, the surface morphology also easily controlled by additional mechanical polishing process. As shown in Figure 2-4, fabricated

NiFe binary alloys (grain size from 20 micrometer and 440 micrometer) were equally have single FCC phase NiFe binary alloys and randomly distributed over the surface, as shown in figure 2-4 (d) and 2-4 (e). The non-poly crystalline structure like X-ray pattern of 440 micrometer gran sized NiFe binary alloy is due to the smaller beam size of X-ray source.

Before compare the grain size contribution to water splitting properties, optimal ratio between Nni and Fe is also measured. NiFe binary alloy with 60 at% Fe shows maximum water splitting properties, as reported.

2-3-2. Electrochemical water splitting properties of micrometer

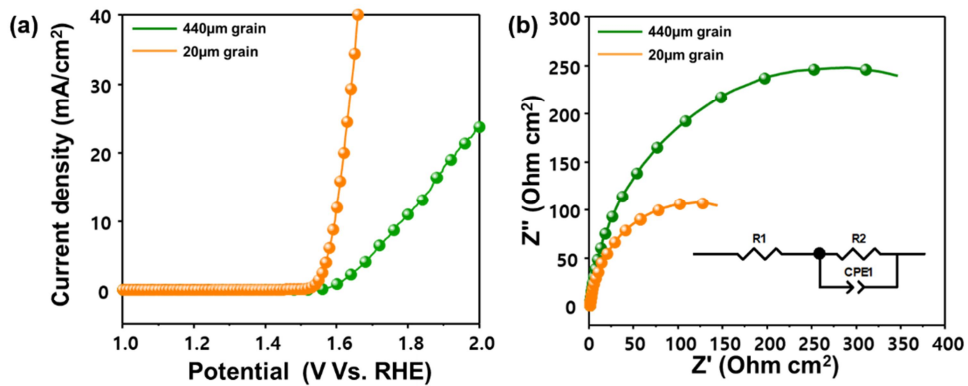


Figure 2-5 (a) Linear sweep voltammograms measured in 1 M NaOH at a scan rate of 10 mV/s for micrometer scale grain sized NiFe binary alloys. (b) EIS measurement of micrometer scale grain sized NiFe binary alloy at 1.5V vs. RHE.

grain size NiFe binary alloys fabricated by arc-melting process

To reveal the contribution of surface grain boundary density to overall oxygen evolution reaction, I employed different grain sized NiFe binary alloys with same composition, morphology, and phase, from 20 micrometer to 440 micrometer grain size. Because the grain size different 20 fold, surface grain boundary density is expected to different about 20 fold. For compare the grain boundary density to water splitting properties, linear sweep voltammograms and EIS measurement is conducted at 1M NaOH solution, using three electrode system.

As expected before, the NiFe binary alloys with 20 micrometer sized grain shows noticeable superb oxygen evolution properties than the NiFe binary alloys with 440 micrometer sized grain. Overpotential for achieve current density of 10 mA/cm² is differ from 552 mV to 370 mV. The EIS measurement of the micrometer scale grain sized NiFe binary alloys was conducted under the 1.5 V Vs. RHE. The larger R_{ct} for large grain NiFe binary alloy indicates that the charge transfer characteristics of the 440 micrometer grain sized NiFe binary alloys are very poor; on the other hand, the 20 micrometer grain sized NiFe binary alloy have a relatively good charge transfer efficiency, exhibiting a low R_{ct} , as displayed in Figure 2-5 (b). We confirmed that the grain boundary at the surface improves the

charge transport efficiency since the EIS plot of 440 micrometer grain sized NiFe binary alloys nanorods indicates large semicircle compared to 20 micrometer grain sized NiFe binary alloy. The linear sweep voltammetry (LSV) curves of our NiFe binary alloys shows dramatic change between small grain and large grain, but the overpotential is still larger than those of reported NiFe binary alloys for achieve current density of 10 mA/cm^2 . Thus, further improvements are needed to generate higher photocurrents.

2-3-3. Electrochemical water splitting properties of nanometer grain size NiFe binary alloys fabricated by pulsed

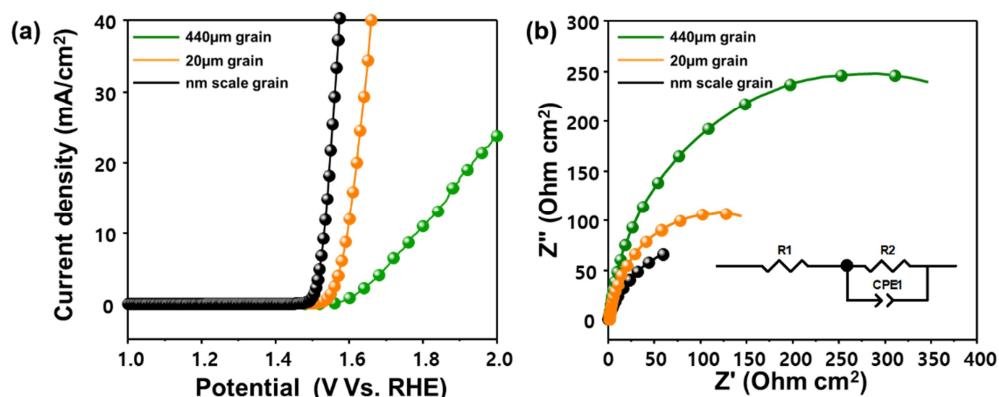


Figure 2-6 (a) Linear sweep voltammograms measured in 1 M NaOH at a scan rate of 10 mV/s for all samples. (b) EIS measurement of NiFe binary alloy at 1.5V vs. RHE for all samples.

electrodeposition

For the extreme compare of grain boundary density, we prepare the nanometer scale grain sized NiFe binary alloys with same composition, phase. Although the direct comparison of NiFe binary alloys synthesized by arc-melting process and electrodeposition process is difficult, at least the slight relation between grain boundary density and oxygen evolution reaction activities can be revealed because the prepared samples are has same composition and same phase, single FCC. The oxygen evolution reaction properties with vary grain size NiFe binary alloys are shown in figure 2-6 (a). As expected above, nanometer scale grain sized NiFe binary alloys show superb oxygen evolution properties than the micrometer scale grain sized NiFe binary alloys, due to the extremely increased surface grain boundary densities. The EIS measurement also shows equal conclusion with those of figure 2-5.

An effective approach to reveal the rate determining step and reaction mechanism change is Tafel plot. Using butler-volmer equation and Tafel slope that measured by linear sweep voltammograms, we could easily

calculate the number of single electron transfer steps prior to the reaction determining step, n' . As calculated from figure 2-7, the number of electro transfer steps prior to the reaction determining step (n') is changed from 0.01 for 440 micrometer grain, 0.33 for 20 micrometer grain to 1.05 for nanometer scale grain sized NiFe binary alloys. In typical charge transfer steps reported for metal hydroxide, the rate determining steps is changed

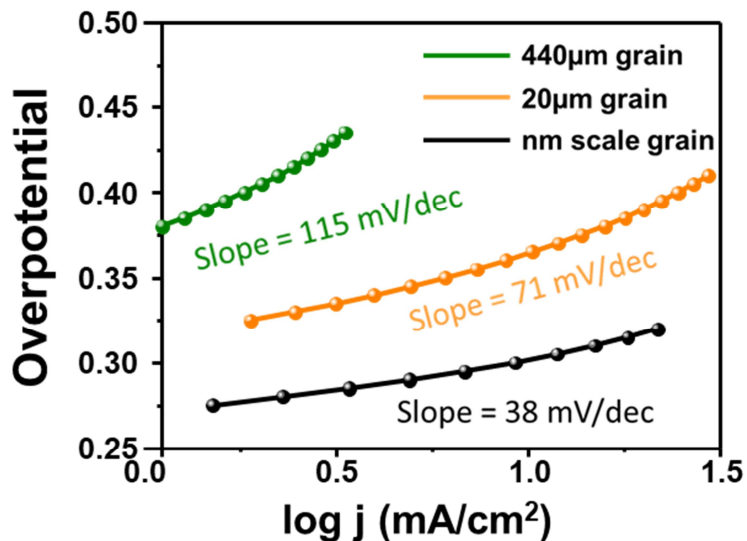


Figure 2-7 Tafel plot of various grain sized NiFe binary alloys. from S_0 to S_1 , indicate that the surface grain boundary density changes bring reaction mechanism change. Furthermore, the reaction mechanism at the grain and grain boundary is differ each other, due to the different OH binding energy at the surface.

- Charge transfer steps (metal hydroxide)

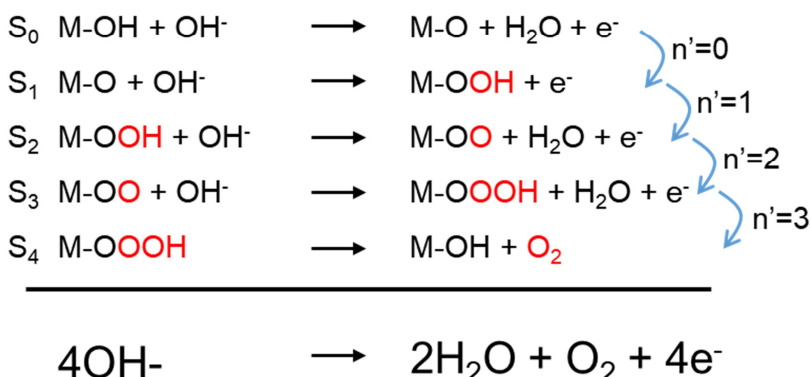


Figure 2-8 Charge transfer steps of typical metal hydroxide.

To more accurate analysis, electrochemical surface area (ECSA) measurement using electrical double layer capacitance is conducted. ECSA measurement is powerful tool to comparison active surface area of electrocatalysts, using electrical double layer capacitance by changing the scan rate at intended measurement voltage range. As measured from 1 V to

1.2 V Vs. RHE, scan rate from 10 mV to 200mV, the double layer

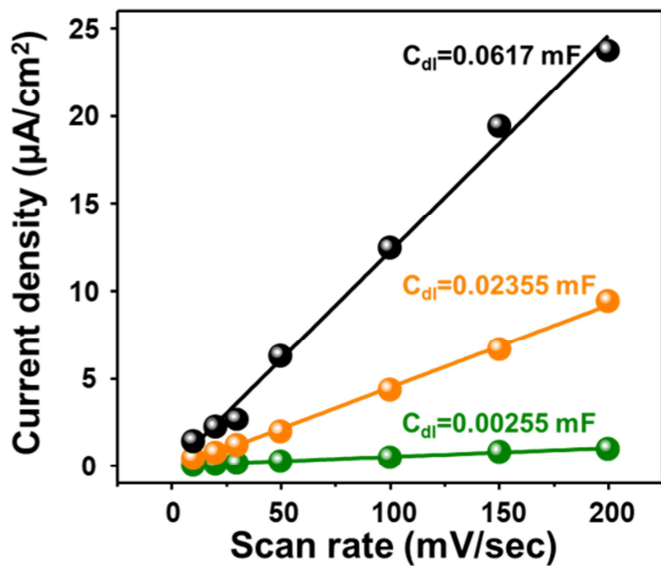


Figure 2-9 Electrochemical surface area measurement using double layer capacitance.

capacitance is remarkably different for NiFe binary samples. As using same theoretical double layer capacitance as a constant, the active surface area of NiFe binary alloys is 25 fold different, as shown in figure 2-9. It also explain the grain boundary act as active sites at the surface, contribute to enhance the overall water splitting properties.

For direct observation of oxygen evolution activity change of grain and grain boundary, scanning photoelectrochemical microscopy (SPECM) measurement is conducted. In-situ observation of oxygen evolution from 1

V to 2 V Vs. RHE, the oxygen evolution reaction is mainly occurred at the grain boundary (figure 2-10). The NiFe binary alloys with nanometer scale grain sized show random-evolution of oxygen bubble, because of large surface grain boundary density. The NiFe binary alloys with 440 micrometer scale grain sized show grain boundary preferred oxygen bubble evolution unlike the nanometer scale grain sized NiFe binary alloy. (Figure 2-10)

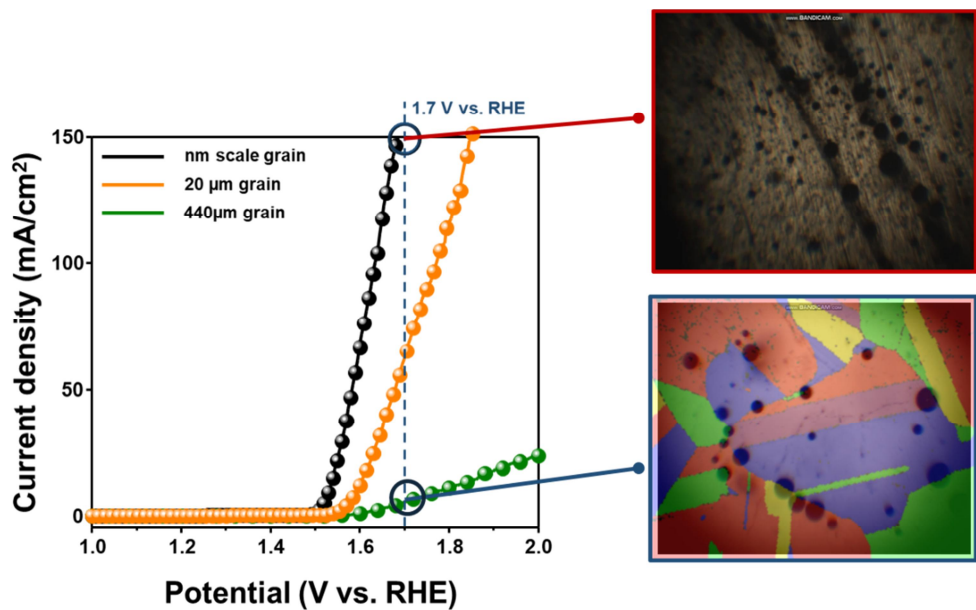


Figure 2-10 SPECM measurement of 440 μm grain and nanometer scale grain NiFe binary alloys.

Those results support the same phenomenon, a critical role of grain boundary density on the oxygen evolution reaction activities. I would like to stress the importance of the optimized composition and conformal surface grain boundary density of metal alloy electrocatalysts to enhance the overall electrochemical water splitting efficiency. Excessive Fe contents of NiFe alloys can deter the effective oxidation of Ni and water oxidation reaction, and deficient Fe contents of NiFe binary alloys has less active sites for efficient water oxidation reaction. Indeed, as grain boundary act as active sites and supply different reaction mechanism at the surface, extremely increased surface grain boundary density with same composition, morphology, and phase have largely enhanced overall water splitting properties than others. In light of the significant improvement in electrochemical water splitting properties, characterization, the optimized composition and grain sized NiFe binary alloy electrocatalyst showed the best performance without additional doping or co-catalysts, and thus may enable enhancement of electrochemical water oxidation.

2-4. Conclusion

I studied various grain sized NiFe binary alloys with same composition, morphology, and phase to identify the correlation of surface grain boundary

density and water splitting reaction activities. It is clear that the grain boundary is more active than the grain and the charge transfer steps are differ between the grain boundary and grain. The optimized atomic ration of NiFe binary alloys with the maximization of surface grain boundary efficiency showed a markedly enhanced current density and reduced overpotential for oxygen evolution reaction. Our approach can be applied to various metal alloy electrocatalysts, in which the OER activity of the oxygen evolution catalysts can be enhanced using an additional dopant or catalyst.

2-5. References

- [1] Middleton, R. S.; Keating, G. N.; Stauffer, P. H.; Jordan, A. B.; Viswanathan, H. S.; Kang, Q. J.; Carey, J. W.; Mulkey, M. L.; Sullivan, E. J.; Chu, S. P.; Esposito, R.; Meckel, T. A., The cross-scale science of CO₂ capture and storage: from pore scale to regional scale. *Energy & Environmental Science* 2012, 5 (6).
- [2] Xiao, Z.; Wang, D.; Dong, Q.; Wang, Q.; Wei, W.; Dai, J.; Zeng, X.; Huang, J., Unraveling the hidden function of a stabilizer in a precursor in improving hybrid perovskite film morphology for high efficiency solar cells. *Energy & Environmental Science* 2016, 9 (3), 867-872.
- [3] Lim, J.; Hörrantner, M. T.; Sakai, N.; Ball, J. M.; Mahesh, S.; Noel, N. K.; Lin, Y.-H.; Patel, J. B.; McMeekin, D. P.; Johnston, M. B.; Wenger, B.; Snaith, H. J., Elucidating the long-range charge carrier mobility in metal

halide perovskite thin films. Energy & Environmental Science 2019, 12 (1), 169-176.

[4] Oh, H. S.; Kim, S. J.; Odbadrakh, K.; Ryu, W. H.; Yoon, K. N.; Mu, S.; Kormann, F.; Ikeda, Y.; Tasan, C. C.; Raabe, D.; Egami, T.; Park, E. S., Engineering atomic-level complexity in high-entropy and complex concentrated alloys. Nat Commun 2019, 10 (1), 2090.

[5] Dai, W.; Lu, T.; Pan, Y., Novel and promising electrocatalyst for oxygen evolution reaction based on MnFeCoNi high entropy alloy. Journal of Power Sources 2019, 430, 104-111.

[6] Lu, Q.; Hutchings, G. S.; Yu, W.; Zhou, Y.; Forest, R. V.; Tao, R.; Rosen, J.; Yonemoto, B. T.; Cao, Z.; Zheng, H.; Xiao, J. Q.; Jiao, F.; Chen, J. G., Highly porous non-precious bimetallic electrocatalysts for efficient hydrogen evolution. Nat Commun 2015, 6, 6567.

[7] George, E. P.; Raabe, D.; Ritchie, R. O., High-entropy alloys. Nature Reviews Materials 2019, 4 (8), 515-534.

[8] Löffler, T.; Meyer, H.; Savan, A.; Wilde, P.; Garzón Manjón, A.; Chen, Y.-T.; Ventosa, E.; Scheu, C.; Ludwig, A.; Schuhmann, W., Discovery of a Multinary Noble Metal-Free Oxygen Reduction Catalyst. Advanced Energy Materials 2018, 8 (34).

- [9] Batchelor, T. A. A.; Pedersen, J. K.; Winther, S. H.; Castelli, I. E.; Jacobsen, K. W.; Rossmeisl, J., High-Entropy Alloys as a Discovery Platform for Electrocatalysis. Joule 2019, 3 (3), 834-845.
- [10] Wang, S.; Xin, H., Predicting Catalytic Activity of High-Entropy Alloys for Electrocatalysis. Chem 2019, 5 (3), 502-504.
- [11] Xia, C.; Jiang, Q.; Zhao, C.; Hedhili, M. N.; Alshareef, H. N., Selenide-Based Electrocatalysts and Scaffolds for Water Oxidation Applications. Adv Mater 2016, 28 (1), 77-85.
- [12] Chua, C. S.; Ansovini, D.; Lee, C. J.; Teng, Y. T.; Ong, L. T.; Chi, D.; Hor, T. S.; Raja, R.; Lim, Y. F., The effect of crystallinity on photocatalytic performance of Co₃O₄ water-splitting cocatalysts. Phys Chem Chem Phys 2016, 18 (7), 5172-8.
- [13] Warren, S. C.; Voitchovsky, K.; Dotan, H.; Leroy, C. M.; Cornuz, M.; Stellacci, F.; Hebert, C.; Rothschild, A.; Gratzel, M., Identifying champion nanostructures for solar water-splitting. Nat Mater 2013, 12 (9), 842-9.
- [14] Yan, Y.; Jiang, C. S.; Noufi, R.; Wei, S. H.; Moutinho, H. R.; Al-Jassim, M. M., Electrically benign behavior of grain boundaries in polycrystalline CuInSe₂ films. Phys Rev Lett 2007, 99 (23), 235504.
- [15] Feng, X.; Jiang, K.; Fan, S.; Kanan, M. W., Grain-boundary-dependent

CO₂ electroreduction activity. J Am Chem Soc 2015, 137 (14), 4606-9.

[16] Feng, X.; Jiang, K.; Fan, S.; Kanan, M. W., A Direct Grain-Boundary-

Activity Correlation for CO Electroreduction on Cu Nanoparticles. ACS Cent Sci 2016, 2 (3), 169-74.

[17] Cai, Q.; Hong, W.; Jian, C.; Li, J.; Liu, W., Insulator Layer Engineering

toward Stable Si Photoanode for Efficient Water Oxidation. ACS Catalysis

2018, 8 (10), 9238-9244.

[18] Zankowski, S. P.; Vereecken, P. M., Electrochemical Determination of

Porosity and Surface Area of Thin Films of Interconnected Nickel

Nanowires. Journal of The Electrochemical Society 2019, 166 (6), D227-

D235.

[19] Wang, Y.; Liu, D.; Liu, Z.; Xie, C.; Huo, J.; Wang, S., Porous cobalt-

iron nitride nanowires as excellent bifunctional electrocatalysts for overall

water splitting. Chem Commun (Camb) 2016, 52 (85), 12614-12617.

[20] Muhunthan, N.; Singh, O. P.; Toutam, V.; Singh, V. N., Electrical

characterization of grain boundaries of CZTS thin films using conductive

atomic force microscopy techniques. Materials Research Bulletin 2015, 70,

373-378.

[21] Deng, B.; Liu, Z.; Peng, H., Toward Mass Production of CVD

Graphene Films. Adv Mater 2019, 31 (9), e1800996.

[22] Cui, X.; Zhang, B.; Zeng, C.; Guo, S., Electrocatalytic activity of high-entropy alloys toward oxygen evolution reaction. MRS Communications 2018, 8 (03), 1230-1235.

Chapter 3

Solution processed electrocatalysts with nanometer scale grain using earth abundant elements for overall water splitting reaction

3-1. Introduction

With the rapid development of industry and population growth, demands for energy are increasing, and the limits of fossil fuels are being revealed. The centuries-old use of fossil fuels has left behind an energy crisis and severe environmental pollution. Thus, the development of sustainable energy resources has become crucial.¹⁻⁶ Compared with other renewable energy resources, solar energy is far more sustainable and abundant, making the conversion of solar energy directly into fuel a promising solution to the current energy crisis. Among the various candidates for green energy resources, hydrogen energy has been the center of attention.⁷⁻⁸ Hydrogen can be generated by a number of techniques such as fossil fuel combustion, biomass, steam reforming or geothermal heating. Amidst many hydrogen

generation techniques, water splitting using photovoltaic–driven electrolysis (PV-EC) is a promising candidate that is environmentally friendly and highly efficient. However, it still remains a great challenge to develop electrocatalysts and photovoltaic devices which generate hydrogen energy with efficiency that is competitive with fossil fuels.⁹⁻¹⁰

Currently, the most efficient catalysts for water splitting are noble-metal catalysts such as Pt-group metals¹¹ and Ru- and Ir-based compounds.¹² Unfortunately, the scarcity and high cost of noble metals seriously impede their large-scale applications in electrocatalytic water splitting. Therefore, more abundant elements are being considered for the role of catalysis. The majority of nonprecious oxygen evolution reaction (OER) catalysts are metal oxides and (oxy)hydroxides.¹³⁻¹⁴ In the past few decades, Ni has emerged as an important nonnoble metal due to its catalytic power for water splitting, with Ni-based compounds being intensively studied as efficient OER¹⁵⁻¹⁶ and HER¹⁷⁻²⁰ catalysts. Among the various types of Ni-based materials, (oxy)hydroxide metal alloys with Fe have attracted much attention due to their special redox characteristics and good accessibility for the reaction species.²¹ To date, the synthesis of NiFe (oxy)hydroxide has relied on hydrothermal,²² pulsed laser ablation (PLAL).²³ Hydrothermal synthesis is a simple method for preparing uniform nanoparticles, but it

typically involves harsh chemical conditions such as a low or high pH, which leads to substrate damage. Although the pulsed laser ablation (PLAL) method has been a simple synthetic route for preparing fine films, the use of vacuum-based equipment is not applicable to industrial processes. For these reasons, direct synthesis from NiFe alloy to NiFe (oxy)hydroxide using anodization can be a simple, economical and clean process for successfully synthesizing uniform films. In addition, the anodization method can be used to simply control the area, surface structure and surface chemistry of the films to serve a desired purpose. Bimetallic electrocatalysts based on Ni have also attracted increasing attention as a reliable approach to enhance electrocatalytic activity for the HER. Meanwhile, inspired by the abundant use of the element Ni in nature, various Ni-based catalysts have been designed to catalyze the conversion of H₂O into H₂ in commercial alkaline electrolyzers. Among these, Ni–Mo alloys are well-known nonprecious-metal electrocatalysts for hydrogen production in alkaline electrolytes because of the increased intrinsic electrocatalysis caused by an appropriate binding energy for hydrogen activity compared to pure Ni.²⁴

The water splitting research conducted hitherto has generally used metal foam or carbon compounds as the bare substrate due to the high conductivity and efficiency of such materials. Here, in this work, instead of

using metal foam, we adopt a NiFe alloy foil as a substrate because well-controlled NiFe alloy shows a superior water splitting performance compared to pure nickel or iron metal. To optimize the catalytic activity, each catalyst was deposited or synthesized in a nanostructured form, and the surface valences were carefully controlled during the synthesis process. Directly synthesized NiFe (oxy)hydroxide showed outstanding OER properties with a low overpotential (250 mV at the OER at 10 mA cm^{-2} in a 1 M NaOH aqueous solution). This is the lowest value among previously reported NiFe (oxy)hydroxide films. Experimental investigations reveal that the synthesized NiFe (oxy)hydroxide behaves as a highly active center and manifests OER kinetics. Electrodeposited NiMo films also exhibit high water splitting properties with a low overpotential (100 mV at 10 mA cm^{-2}) and low Tafel slope (22.2 mV per decade) in a 1 M NaOH aqueous solution, which are comparable to those of a Pt plate (10 mA cm^{-2} overpotential: 130 mV; Tafel slope: 19.1 mV per decade).²⁷ With these highly efficient electrocatalysts in hand, the next step was to combine them with a solar cell for the purpose of directly converting solar energy into the form of an energy source, namely, hydrogen. Our photovoltaic-electrochemical (PV-EC) cells connected by metal wires were found to exhibit a solar-to-hydrogen efficiency of 17.52% under simulated AM 1.5G solar irradiation

(100 mW cm⁻²), which is superb compared to reported articles, as many advantages like;

1. Facile and low cost synthesis

Metal (oxy)hydroxide is regarded as a promising water splitting catalysts, because of the unique physical and chemical properties. Specially Ni based (oxy)hydroxides have been widely investigated with superior activities comparable to the noble metal based catalysts like platinum, ruthenium oxide or iridium oxide. To date, the synthesis of NiFe (oxy)hydroxide has mainly relied on hydrothermal or pulsed laser ablation, which require toxic chemicals and high-cost process. For this reasons, existing synthesizing methods has limitation in practical industrial application. Here in this work, we overcome the current problems by applying fully solution- based processes (anodization for the oxygen evolution catalyst and electrodeposition for the hydrogen evolution catalyst) for simple, economical process. Roll-to-roll process for NiFe alloy synthesis and anodization, electrodeposition method for electrocatalysts that we used were promising technique because it could easily control the thickness and active surface area of films.

2. State-of-art OER & HER catalytic properties

Highly active catalysts for the water splitting are required for the efficient hydrogen production. To achieve superior activities, each catalyst should have fast charge transportation rate and large active surface area. By using anodization and electrodeposition, we could achieve optimized conductivity and surface morphology that maximizing the water splitting properties of catalysts. NiFe (oxy)hydroxide synthesized by an anodization method for the OER catalyst shows an overpotential of 250 mV at 10 mA cm⁻², which is dramatically smaller than that of bare NiFe alloy with an overpotential of 520 mV at 10 mA cm⁻². Electrodeposited NiMo films for the HER catalyst also exhibit a small overpotential of 100 mV at 10 mA cm⁻² compared with that of bare NiFe alloy (550 mV at 10 mA cm⁻²). Two-electrode cell also shows outstanding performance than as reported many articles, an extremely small overpotential of 390 mV at 10 mA cm⁻².

3. Remarkable solar-to-hydrogen efficiency

In terms of practical performances, two electrode cell combining with photovoltaic devices could be a fine way to evaluate the efficiency of water splitting catalysts. In this work, water splitting experiments using solar energy were performed with monolithic perovskite/Si tandem cells. These tandem cells exhibit a very suitable open-circuit voltage for the water splitting (around ~1.7 V) because the maximum photocurrent density can be

collected near 1.5 V. Using the tandem cell exhibited a high PCE of 23.1%, operating current density of the combined system achieve a value of 14.24 mA cm^{-2} . Taking $\eta_F = 100\%$ and $J_{sc} = 14.2 \text{ mA cm}^{-2}$, the STH efficiency was determined to be 17.52%. Compared with other recently reported PV-EC systems, our system is comparable to state-of-the-art solar water splitting systems in terms of the solar-to-hydrogen efficiency (STH) and the solar-to-hydrogen efficiency per photocurrent-to-charge efficiency (STH/PCE).

3-2. Experimental method and characterization

3-2-1. Synthesize of NiFe alloy

Figure 3-1 and 3-2 shows an illustration of our synthesizing methods for forming NiFe (oxy)hydroxide and Ni₄Mo films on the as-prepared NiFe alloy used in this study. All of the process to synthesize electrocatalysts used in this work were based on fully solution method, facile and low cost process. Solution process also has many advantages like easy control of the

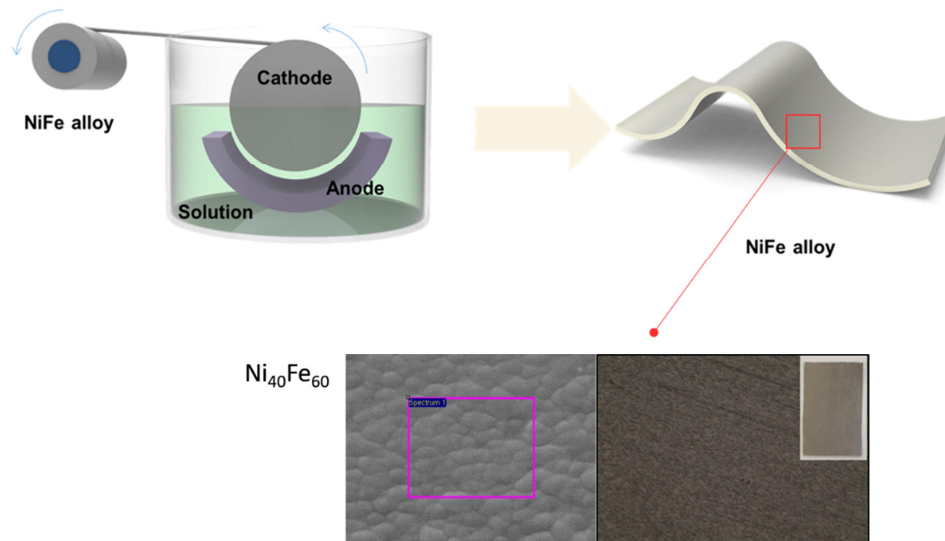


Figure 3-1 Sketch diagram of electroforming process to make an NiFe alloy foil. Cathode electrode was rolling with continuous supplied bath solution, NiFe alloy foil are deposited on the other side of electrode coil. surface morphology, flexibility and scale of the materials. NiFe alloy used in this work were synthesized by roll-to-roll process.

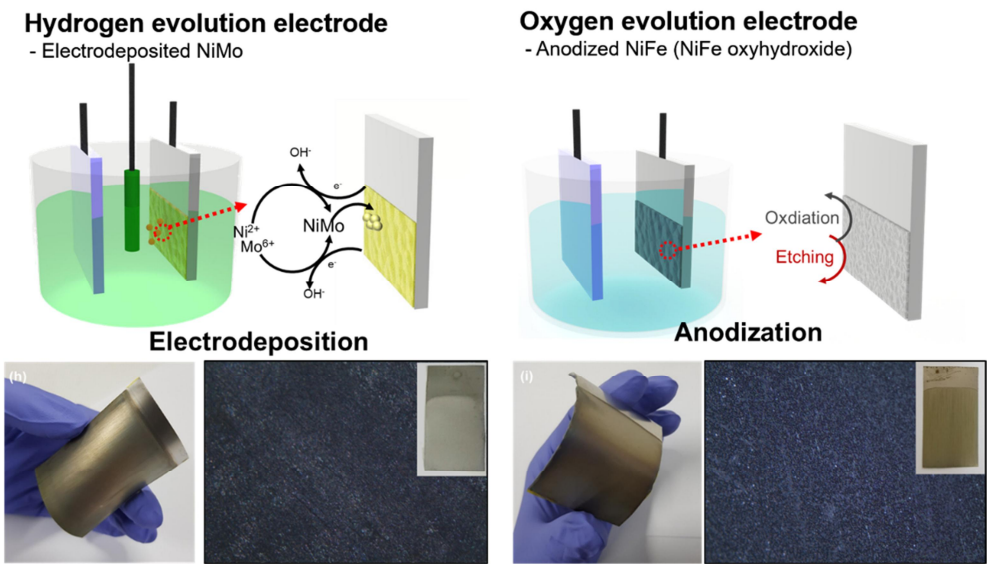


Figure 3-2 Illustrated sketch of our synthesis procedure for forming a water splitting cell. The cathode material was deposited onto the NiFe alloy by using an electrodeposition method, and the anode material was obtained simply by anodizing the NiFe alloy. The key idea of our method is the direct anodization of the metal alloy substrate for the synthesis of more efficient electrodes with long-term stability.

3-2-2. Synthesize of NiFe (oxy)hydroxide and NiMo

NiFe (oxy)hydroxide on the NiFe alloy was synthesized via a direct anodic oxidation process. Prior to the anodization, the NiFe alloy with a size of 20 mm × 10 mm was ultrasonically degreased in acetone and ethanol, rinsed with DI water and then finally dried in air. The anodization was carried out in a conventional two-electrode electrochemical cell with the NiFe alloy

used as a working electrode and platinum foil used as a counter electrode at room temperature. All of the samples were formed by simply anodizing the NiFe alloy in ethylene glycol containing 0.3 wt % NH₄F solution and 3 vol % water at a constant voltage. The NiFe(oxy)hydroxide films on the NiFe alloy show a slightly yellowish nanoporous structure after anodization. After anodization, the samples were immediately rinsed with DI water and subsequently dried in air. Ni₄Mo alloy was synthesized by a direct electrodeposition method. Briefly, the electrodeposition process was performed on the as-prepared NiFe foil in an electrolyte containing 0.017 M nickel sulfate, 0.016 M sodium citrate, 0.00036 M ammonium molybdate and 0.285 M sodium chloride at a cathodic voltage of 1.2 V for 60 min. The pH of this electrolyte was adjusted at 8.5 by ammonium hydroxide, and the temperature was elevated to 50 °C with continuous stirring. After electrodeposition, the NiFe foil was covered by a gray metal film.

3-2-3. Fabrication of the monolithic perovskite/Si solar cells

Perovskite/Si tandem solar cells was synthesized simply with the previous paper.⁴⁶ Both sides of 250-μm-thick n-type phosphor-doped Si wafers prepared by a floating zone technique were polished and sequentially cleaned using an RCA cleaning process. The Si-substrates had only a back-side-textured structure. After immersion into a HCl:H₂O₂ and H₂SO₄:H₂O₂

solution to eliminate contaminants, the substrates were cleaned with deionized water. Then, 10–20-nm-thick-doped amorphous Si thin films were deposited on both sides of the Si substrate using a plasma-enhanced chemical vapor deposition reactor operating at radio frequency (RF 13.56 MHz). To dope the a-Si:H, hydrogen-diluted PH₃ and B₂H₆ gases were used as sources. As a recombination layer, a 20-nm-thick ITO layer was deposited using a radio-frequency (RF) sputtering method with a power of 50 W under a working pressure of 2 mTorr at room temperature. For the deposition of NiO as a hole extraction layer, 0.1 M nickel(II) acetate tetrahydrate solution was spin-coated onto Si-cells and annealed at 220 °C for 1 h. The substrates were moved to a N₂-filled glove box (O₂ and H₂O less than 1 ppm) for the deposition of perovskite films. A total of 100 μL of the perovskite solution containing 1.275 mmol of PbI₂ (Alfa Aesar, 99.9985%), methylammonium iodide (Greatcellsolar) and 0.225 mmol of PbBr₂ (Sigma-Aldrich, 99.999%), methylammonium bromide (Greatcellsolar) in 1 mL of a mixed solvent (DMF : DMSO = 9:1 v/v) was spin-coated onto the prepared substrates. During spinning, Diethyl ether (Daejung, ≥99.9% purity) was poured onto the substrate. Then, the perovskite films were annealed at 100 °C for 30 min. A [6,6]-phenyl-C₆₁-butyric acid methyl ester ([60] PCBM, nano-C, 99.5% purity) solution (25

mg mL⁻¹ in 1,2-dichlorobenzene) and a ZnO nanoparticle ink (Sigma-Aldrich) were sequentially spin-coated onto the perovskite films as electron-extraction layers. A 150-nm-thick layer of ITO film was deposited by the same conditions with a recombination layer, and a 150-nm-thick layer of Ag metal electrode deposited by thermal evaporation at a deposition rate of 1.5 Å/s.

3-2-3. Physical characterization

The XRD data were acquired using a BRUKER MILLER Co., D8-Advance diffractometer with Cu K α radiation ($\lambda = 1.5406 \text{ \AA}$) operating at 45 kV and 200 mA at a scanning rate of 0.06° sec⁻¹. The surface and cross-sectional images were obtained from a field emission scanning electron microscope (ZEISS, MERLIN Compact) and transmission electron microscope (TEM) JEOL JEM 3000F. X-ray photoelectron spectroscopy (XPS) measurements were carried out using KRATOS_AXIS-His and a monochromated Al-K α ($h\nu = 1486.58 \text{ eV}$) X-ray source to determine the composition of the synthesized rod. The high-resolution spectra of the Ni 2p, Fe 2p, Mo 3d, O1s, and C1s core levels were identified using a pass energy of 100 eV through a 0.4 mm analyzer slit width. Each high-resolution scan was measured four times and then summed using 50 meV steps with a dwell

time of 157 ms per step. The $J-V$ measurements were performed using a potentiostat (CHI 608C, CH Instruments) and a solar simulator (Peccell Technologies, AAA graded) under AM 1.5G illumination conditions. The solar simulator was used after calibration with a reference cell (PV Measurements). The aperture size defined by the metal mask was 0.1875 cm².

3-2-4. Electrochemical characterization

: All water splitting performance measurements except for the two-electrode system were carried out in a three-electrode configuration consisting of the as-prepared working electrode, calomel reference electrode, and a Pt wire as a counter electrode with 1 M NaOH electrolyte solution, with the pH of the electrolyte considered to be 14. All potentials were applied versus a 3 M Ag/AgCl reference electrode and converted into the reversible hydrogen electrode (RHE) based on the Nernst equation:

$$V_{RHE} = V_{Ag/AgCl} + E_{Ag/AgCl} + 0.059 \times pH$$

where V_{RHE} and $V_{Ag/AgCl}$ are the applied potentials against the RHE and 3 M Ag/AgCl reference electrode, respectively. The current was recorded

using a computer-controlled multichannel electrochemical analyzer potentiostat (IVIUM STAT), which was used to simultaneously control the potential. EIS spectra were recorded using the same potentiostat in the preceding three-electrode configuration. A sinusoidal voltage perturbation with an amplitude of 10 mV and frequencies ranging from 350 kHz to 1 Hz was superimposed onto the bias voltage to gather the EIS data. The EIS data were fit to the equivalent circuits. Faradaic efficiency and hydrogen/oxygen evolution rates were measured by using gas chromatography (GC) at a constant current density of approximately 10 mA cm^{-2} .

3-3. Results and discussion

3-3-1. Structure characterization of the NiFe (oxy)hydroxide and

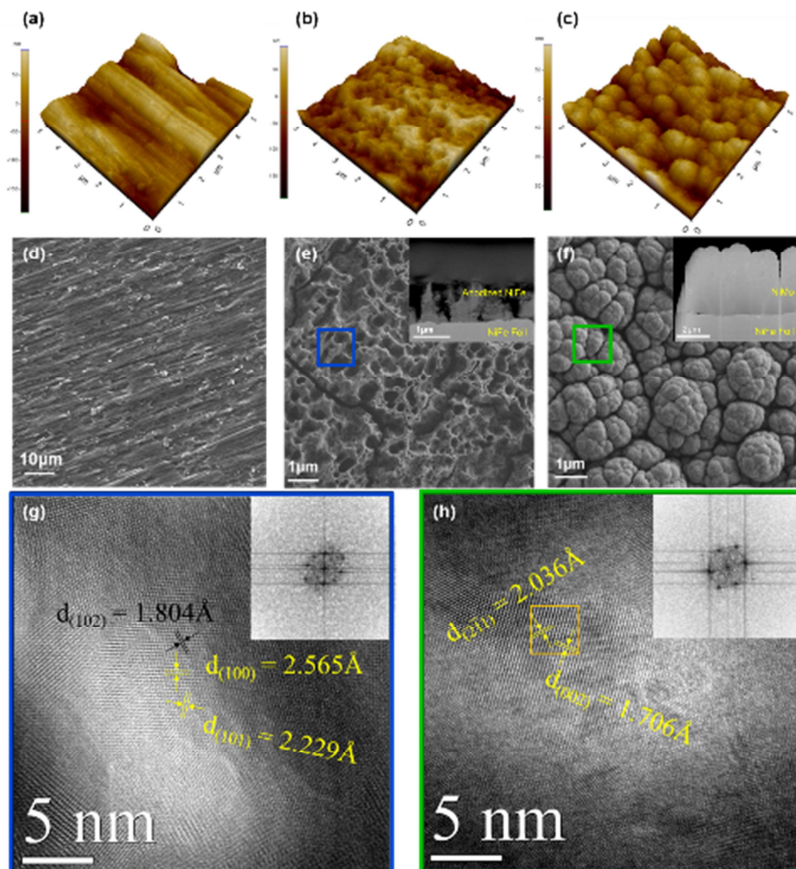


Figure 3-3 Structural characterization of the NiFe alloy, NiFe (oxy)hydroxide films and Ni₄Mo films on the NiFe alloy. (a), (b), (c) 3-dimensional atomic force spectroscopy images of bare NiFe alloy, NiFe (oxy)hydroxide films, and Ni₄Mo films. (d), (e), (f) SEM images of bare NiFe alloy, NiFe (oxy)hydroxide films, and Ni₄Mo films, respectively. The high-resolution TEM images of (g) NiFe (oxy)hydroxide and (h) Ni₄Mo film. The SAED patterns for the synthesized films are displayed in the

NiMo films

The structure and morphology of NiFe (oxy)hydroxide and Ni₄Mo were characterized with a number of techniques. Three-dimensional AFM images clearly showed a microporous surface for the NiFe (oxy)hydroxide (Figure 3-3 b) and nanostructured Ni₄Mo film (Figure 3-3 c) compared to the NiFe alloy (Figure 3-3 a). The morphologies of NiFe (oxy)hydroxide and Ni₄Mo were examined by scanning electron microscopy (SEM) as shown in Figure 2d-2f. The anodization of NiFe alloy effectively leads to formation of microporous NiFe (oxy)hydroxide films with pore size in range of 0.5 – 1.0 μm, as shown in Figure 3-3 c. NiFe (oxy)hydroxide films with extensive, numerous pores can be acted as an active surface for water splitting reactions and contributed to enhancing the OER performance. Cross section image (inset of Figure 3-3 e) shows the thicknesses of the NiFe (oxy)hydroxide films to be approximately 2 μm. The Ni₄Mo film deposited on the NiFe alloy (Figure 3-3 f) showed an isolated hemispherical structure with abundant protrusions, which is possible to provide enlarged active areas during the HER. The wide, open spaces between adjacent nanostructures and the coarse surface allowed fast ion diffusion and enlarged the contact area with electrolyte, which were both beneficial for improving the HER performance. The crystalline structure of the NiFe alloy, NiFe (oxy)hydroxide and Ni₄Mo films deposited on the NiFe alloy were

characterized by X-ray diffraction (XRD). The NiFe alloy deposited by roll-to-roll process at room temperature consists of a mixture of fcc and bcc phases, as evidenced from the X-ray diffraction (XRD) pattern, which shows fcc (111) and bcc (110) peaks with the strongest intensities at 43.7° and 44.7° . The NiFe (oxy)hydroxide shows apparent NiFe (oxy)hydroxide X-ray diffraction peaks compared to the bare NiFe alloy, but the electrodeposited Ni_4Mo films was not shows marked X-ray diffraction patterns, due to the intensify high XRD peak of NiFe alloy (Supplementary Figure S3).²⁵ High-resolution transmission electron microscopy (HRTEM) was carried out to further analyze the phase and structure of NiFe (oxy)hydroxide (Figure 3-3 g) and Ni_4Mo films (Figure 3-3 h). The smudgy selected area diffraction (SAED) pattern (inset of Figure 3-3 g) is due to the low crystallinity of the anodizing method; however, the lattice spacing clearly showed a polycrystal phase for $\text{Ni}(\text{OH})_2$ and NiFe (oxy)hydroxide. Figure 2g shows a lattice spacing of 0.1804 nm for the nanostructure corresponding to the (101) plane of $\text{Ni}(\text{OH})_2$ (JCPDS:014-0117) and lattice spacing of 0.256 nm and 0.2229 nm corresponding to the (100) plane and (101) plane, respectively, of $(\text{Ni}_{0.33}\text{Fe}_{0.67})\text{OOH}$ (JCPDS:014-0556). It is clear that a NiFe (oxy)hydroxide layer was successfully formed by anodization. The HRTEM image and SAED pattern (Figure 3-3 h) indicate

that the electrodeposited films are suitably matched to Ni₄Mo (JCPDS:007-0562 with lattice spacing of 0.2036 nm and 0.1706 nm corresponding to the (211) and (002) planes, respectively. Diverse analysis equally concluded that NiFe hydroxide/NiFe oxy(hydroxide) and Ni₄Mo films were successfully synthesized by the anodization method and electrodeposition, respectively.

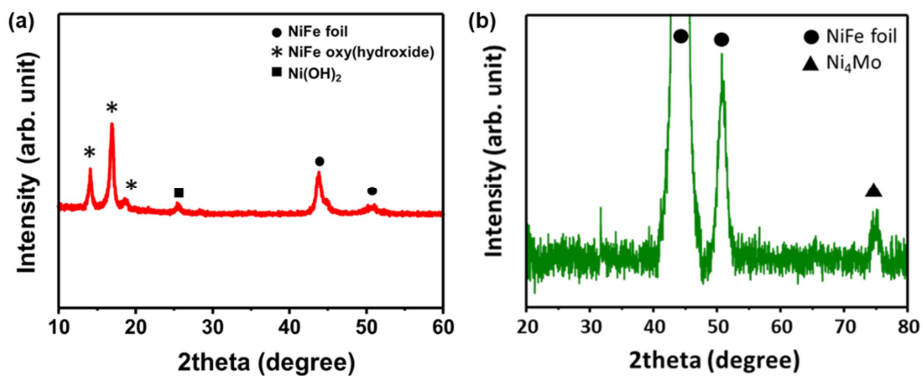


Figure 3-4 XRD characteristics of the NiFe (oxy)hydroxide films and electrodeposited NiMo films.

3-3-2. Electrocatalytic oxygen and hydrogen evolution reaction

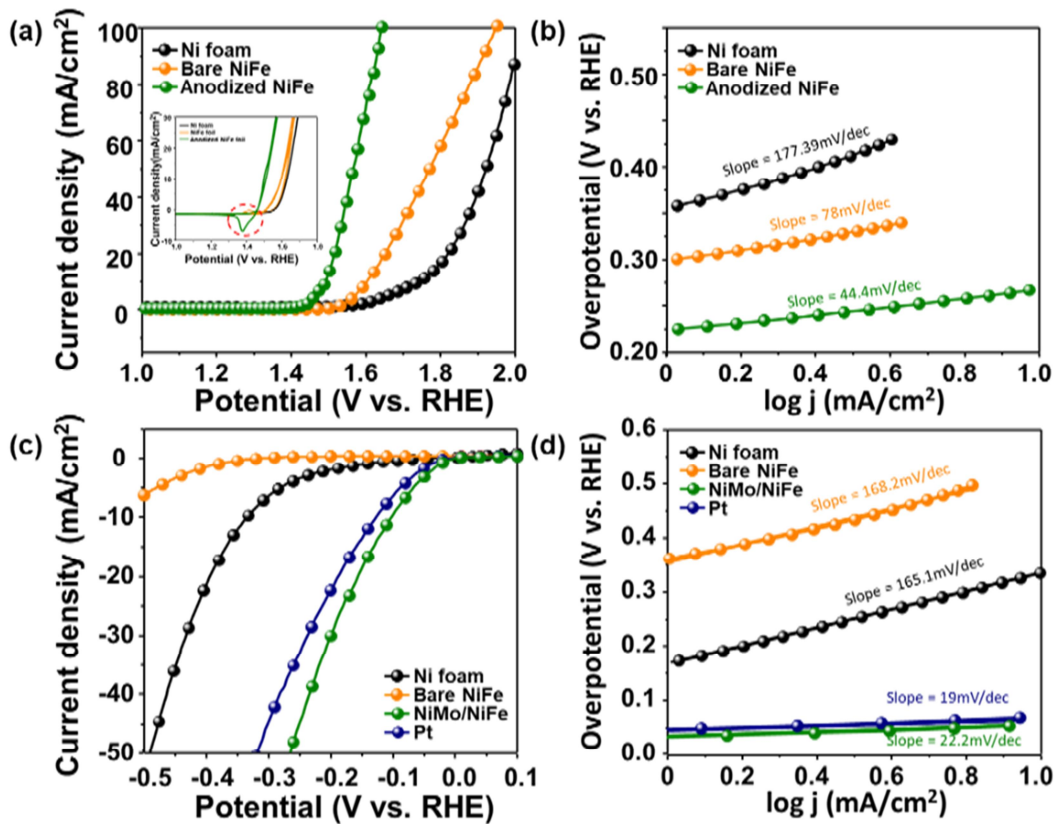


Figure 3-5 Electrochemical performance of different catalyst electrodes as characterized by linear sweep voltammetry in 1 M NaOH aqueous electrolyte. (a) OER characteristics of different catalyst electrodes in a three-electrode configuration scanned in the direction from the positive to the negative potential on the RHE scale. (b) Tafel slopes for the OER electrode and (c) HER characteristics for the different catalyst electrodes in a three-electrode configuration scanned in the direction from the negative to the positive potential. (d) Tafel slopes for the HER electrode. All scan rates were 1 mV s^{-1} .

In order to understand how the structure and phase affect the water splitting properties, we evaluate the electrocatalytic activities of the electrocatalysts by three-electrode system in a 1 M NaOH aqueous solution using a 3 M Ag/AgCl electrode and a platinum plate as the reference and counter electrodes, respectively. All potentials were referenced to the reversible hydrogen electrode (RHE), and the ohmic potential drop loss from the electrolyte resistance was subtracted. At first, a pure nickel foam was tested to compare the OER performance of the bare NiFe alloy. For the optimized pore size and conductivity of films, various anodizing conditions were tested. As revealed in Figure, the NiFe (oxy)hydroxide film anodized at the potential of 80V exhibited the highest OER activity, with a lowest overpotential at current density 10 mA cm^{-2} . As displayed in Figure 3a, the NiFe alloy showed a superior OER performance to the nickel foam due to the disparity in active surface area for water splitting reaction. The active surface area is one of the dominant factors that directly influences the activity of the electrocatalyst. Thus, a synergetic effect between Ni and Fe can not only offset the surface area shortage but also achieve a better water splitting performance for the NiFe alloy than the Ni foam at the OER. The OER performance of NiFe (oxy)hydroxide films (overpotential of 250 mV at a current density of 10 mA cm^{-2}) is considerably enhanced compared to

the bare NiFe alloy (380 mV) and nickel foam (520 mV). Cyclic voltammetry curves (inset of Figure 3a) show a noticeable peak change between the NiFe alloy and NiFe (oxy)hydroxide. The green reduction peak in the red circle, as shown in Figure 3a represents a phase change from NiO(OH) to Ni(OH)_2 .²⁶ As shown in the cyclic voltammetry curves, the NiFe (oxy)hydroxide films has a high rate of Ni^{3+} compared to the bare NiFe alloy, it is a crucial evidence that can demonstrate phase change from NiFe alloy to NiFe (oxy)hydroxide films after anodization. Usually, NiFe (oxy)hydroxide and metal (oxy)hydroxide electrocatalysts show superior water splitting properties to metal oxide or pure metal electrocatalysts due to their special redox characteristics and good accessibility for the reaction species,²⁷⁻³⁰ which can be the main reason for the enhanced OER properties of the NiFe (oxy)hydroxide films. The superior OER performance of the NiFe (oxy)hydroxide films was also confirmed by its smaller Tafel slopes as derived from LSVs (44.4 mV dec^{-1} , Figure 3b) compared to the other samples, such as the NiFe alloy (78 mV dec^{-1}) and Ni foam ($177.39 \text{ mV dec}^{-1}$). A smaller Tafel slope indicates that a faster active reaction occurs on the surface of an electrocatalyst than on that of another.

Furthermore, the HER performance was also tested. (Figure 3c). At first, series of electrodeposited NiMo films were investigated to optimize the

synthesizing conditions. As revealed in Figure S6, the NiMo alloy electrodeposited at the temperature of 60 degree, voltage of 2.5 V, deposition time of 1 hour exhibited the highest HER activity. For an objective comparison, a Ni foam and a Pt plate were also prepared. Unlike the OER, the bare NiFe alloy shows an inferior HER performance to the nickel foam. To drive overall water splitting system, HER performance should be improved, thus a Ni₄Mo film was deposited onto the NiFe alloy, as a HER catalyst. The electrocatalytic performance of the Ni₄Mo film for the HER was tested in 1 M NaOH. At a current density of 10 mA cm⁻², the Ni₄Mo film exhibits the smallest overpotential of 100 mV compared to the other samples, including the Ni foam (370 mV) and bare NiFe alloy, which is even better than that obtained for the pure Pt (130 mV) electrode. Figure 3d displays the Tafel plots for the corresponding polarization curves, which provide profound insights into the fundamental HER kinetic mechanisms occurring on the surfaces of the electrocatalysts. As a result of the low energy barrier (0.44 eV on Pt) for the Volmer step, the kinetic rate-limiting step for the Pt catalyst is the Tafel process, with the theoretical Tafel slope being 30 mV per decade. Remarkably, the Tafel slope for the Ni₄Mo film was as low as 20 mV per decade, which is far lower than the values of 165 mV per decade and 168.2 mV per decade obtained for the Ni foam and

bare NiFe, respectively, and is highly comparable to that of the Pt-based catalyst. This result indicates that the electrocatalytic HER kinetics on the Ni₄Mo electrocatalyst were determined by the Tafel step rather than a coupled Volmer–Tafel or Volmer–Heyrovsky process. In other words, the prior Volmer step was significantly accelerated. Additionally, except for the excellent water electrolysis properties, both OER and HER electrodes also exhibits a high stability during 200 cycle CV tests (Supplementary Figure S7), almost same after 200 cycles. This catalysts were shown superior water splitting activity than other reported non-noble metal based electrocatalysts, even comparable to that of the noble metal based catalysts like Platinum or Iridium oxide. (Supplementary Figure S8). To test the overall water splitting, a two-electrode cell was constructed by using NiFe (oxy)hydroxide as the anode and a NiMo alloy as the cathode. A photograph (Figure 4b) and corresponding movie (supplementary Movie 1) reveal that at an applied cell voltage of 1.6 V, a large amount of H₂ gas evolves at the cathode, and O₂ gas bubbles evolve at the anode. The electrolytic cell demonstrated excellent catalytic activity; it can deliver a current density of 10 mA cm⁻² at a voltage of only 1.62 V (Figure 4a), which is 110 mV smaller than that required when using the Ni foam as both the cathode and anode, and 80 mV smaller than that previously reported for Ni-LDH/Ni-foam in a two-electrode

configuration.³¹ Even more, efficient water electrolysis can be powered by a single-cell 1.5 V AAA battery, (Figure 4) and superior that of as reported electrolysis cells.³² Supplementary movies showing hydrogen bubbles was vigorously occurred by 1.5 V AAA battery. This results indicate that our NiFe (oxy)hydroxide/Ni₄Mo water splitting electrode has good possibility for practical applications.

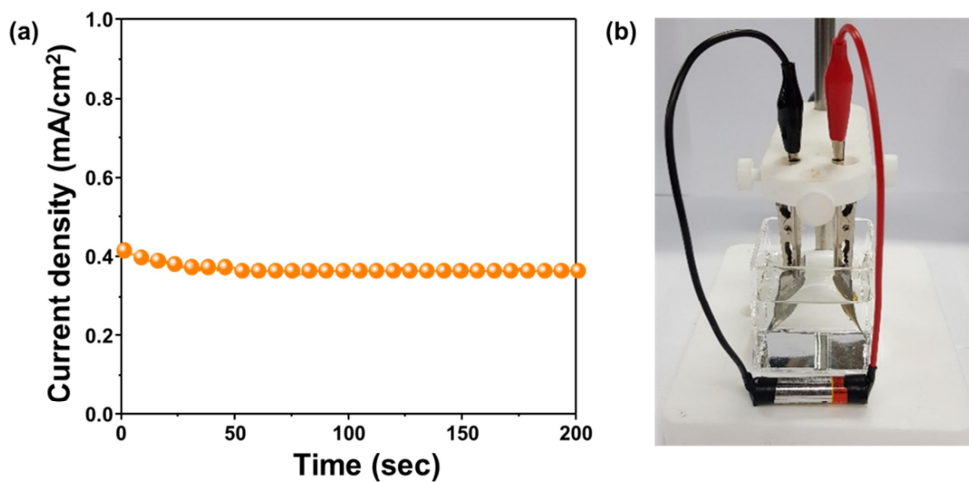


Figure 3-6 2 electrode water splitting properties combining with a conventional 1.5 V battery. (a) Current density and (b) NiFe (oxy)hydroxide/NiMo water splitting system driven by an ~1.5 V AAA battery.

3-3-3. Characterization of the NiFe (oxy)hydroxide and NiMo electrocatalyst

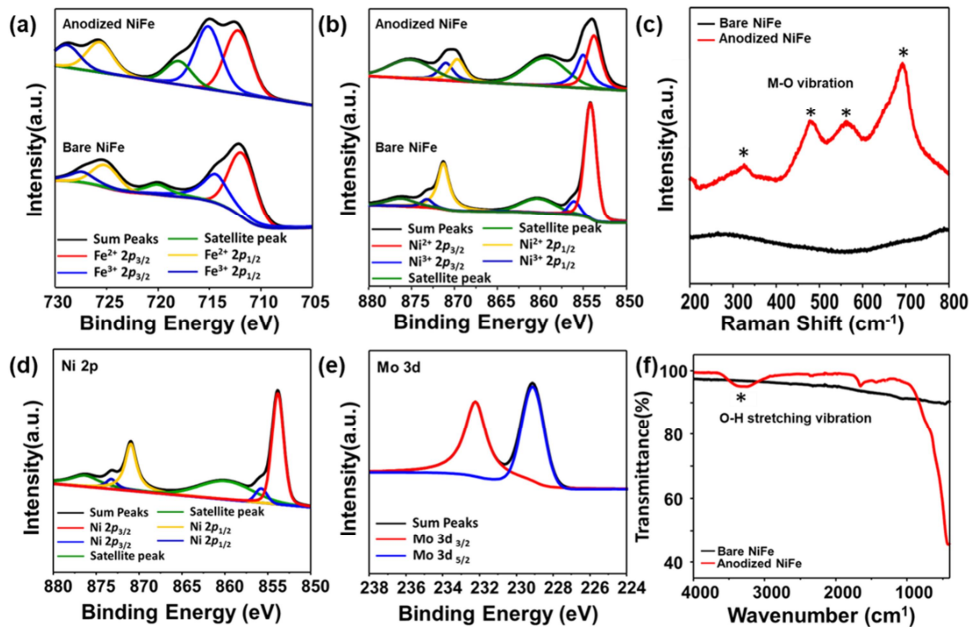


Figure 3-7 Chemical characterization of the NiFe (oxy)hydroxide and Ni₄Mo electrocatalysts. (a) and (b) XPS spectra for Fe and Ni before and after anodization. (c) Raman spectra for the bare NiFe alloy and NiFe (oxy)hydroxide films, (f) FT-IR spectra for the bare NiFe alloy and NiFe (oxy)hydroxide films. (d) and (e) the Ni and Mo XPS spectra for the Ni₄Mo films.

The surface compositions and valence states were investigated by X-ray photoelectron spectroscopy (XPS) to evaluate exact reasons of enhanced activity. Peak fitting analysis for Ni 2p in the as-prepared NiFe alloy (Figure

5b) indicated the presence of Ni²⁺ (855.4 eV and 873.1 eV) and Ni³⁺ (857.3 eV and 875.5 eV)³³⁻³⁴. The Ni 2p spectra for the as-prepared NiFe alloy originated from the native oxide layer on the surface of the NiFe alloy. Compared to the as-prepared NiFe alloy, peak fitting analysis for Ni 2p in the NiFe (oxy)hydroxide film indicated a shift to lower energies with the Ni³⁺ peaks relatively increased, suggesting that NiOOH was formed on the surface by the anodization method. For the Fe 2p spectra, there were two dominant peaks due to Fe²⁺ (712.5 eV) and Fe³⁺ (714.0 eV), which originated from the native oxide layer on the surface of the NiFe alloy (Figure 5a).³⁵⁻³⁶ For the case of the NiFe (oxy)hydroxide film, the strong Fe³⁺ peak was intensified, indicating the formation of either Fe₂O₃ or FeOOH on the surface. O 1s regions of the XPS spectra were also examined to identify the bonding types for metal and oxygen. The XPS spectra showed two peaks due to lattice oxygen bonds (O-M, 530.1 eV) and hydroxide or oxyhydroxide groups (M-OH or M-OOH, 531.7 eV).³⁷⁻³⁹ The as-prepared NiFe alloy shows relatively low O 1s XPS spectra with similar intensities for the M-OH and O-M bonds. In contrast, the major oxygen component in the NiFe (oxy)hydroxide film was found to be either the M-OH or M-OOH groups.

Further examinations of Raman spectroscopy and a Fourier transform

infrared spectrometer (FT-IR) reveal the chemical state of the NiFe catalyst. Raman spectra were collected from 200 to 800 cm⁻¹. The peaks at 480 cm⁻¹, 562 cm⁻¹ and 693 cm⁻¹ assigned to the vibrations of NiFe–O,⁴⁰ which is clearly signify the surface of the NiFe (oxy)hydroxide was partially oxidized by anodization. The presence of NiFe (oxy)hydroxide films is also confirmed by analyzing the FT-IR spectra (Figure 5f). In contrast to the flat FT-IR spectra of the bare NiFe alloy, (oxy)hydroxides shows a broad absorption band spectra between 3500 cm⁻¹ and 3000 cm⁻¹ corresponding to the O–H stretching vibrations of the hydroxyl groups in the hydrotalcite layers and interlayer water molecules, respectively.⁴¹ From these results, it can be concluded that an amorphous NiFe (oxy)hydroxide layer was conformally formed by anodization. Raman spectroscopy for the Ni₄Mo films also indicate the formation of Ni₄Mo films after the electrodeposition.

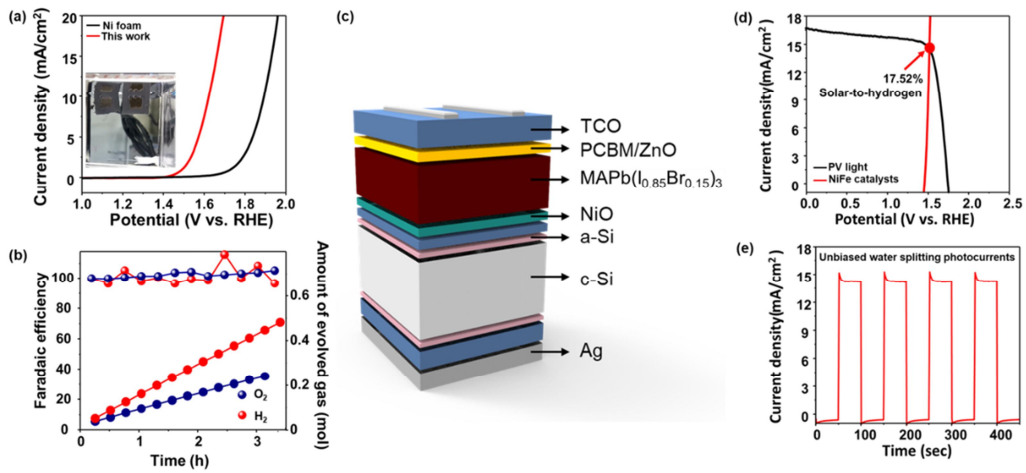


Figure 3-8 Combination of the silicon tandem cell with NiFe (oxy)hydroxide/NiMo electrodes for water splitting. (a) Overall water splitting characteristics versus Ni foam in a two-electrode configuration scanned from 2.0 V to 1.0 V. (b) Faradaic efficiency of the water splitting electrode. (c) Schematic diagram of the water splitting device. (d) J - V curves for the silicon tandem cell and the NiFe LDH/NiMo electrodes in a two-electrode configuration under AM 1.5G 100 mW cm^{-2} illumination. The aperture size of the tandem cell was 0.1875 cm^2 , and the catalyst electrode areas were $\sim 2 \text{ cm}^2$ each. (e) Current density–time curve of the integrated water splitting device without external bias under chopped simulated AM 1.5G 100 mW cm^{-2} illumination.

3-3-3. Solar-to-hydrogen efficiency

To drive our electrolysis system based on earth-abundant electrocatalysts with solar irradiation, monolithic perovskite/Si tandem solar cells were combined as the light harvesting materials. Figure 6C briefly shows the

structure of the tandem solar cell used in this work. These tandem cells exhibit sufficiently high open-circuit voltage for the water splitting (around ~ 1.7 V) because the maximum photocurrent density can be collected near 1.5 V. The precise control of the band gap, which influence in current density and photovoltage of the solar cell, via compositional engineering such as Br-incorporation into the X-site is a representative strong point of perovskite materials. We chose Br doped methylammonium lead iodide ($\text{MAPb}(\text{I}_{0.85}\text{Br}_{0.15})_3$) as the composition for the light absorber layer to achieve a high V_{oc} .

Figure 6d shows the electrolysis current and corresponding STH efficiency for the perovskite/Si tandem solar cells. The STH efficiency of the coupled system is calculated according to the following equation⁴²

$$\text{STH} = \left[\frac{(1.23 - V_{app}) \times J_{sc} \times \eta_F}{P_{in}} \right]_{AM\ 1.5G}$$

where J_{sc} is the short-circuit current of the PV-coupled electrolysis system (measured at standard AM 1.5G insolation conditions), η_F is the Faradaic efficiency, 1.23 V is the reversible voltage (V_{rev}) of the water splitting reaction (at 25°C), and P_{in} is the power density of the incident light (100

mW cm^{-2}). Using the above-demonstrated high-efficiency, low-cost water splitting catalyst and perovskite/Si tandem solar cells, an overall water splitting cell was assembled. The tandem cells were placed outside of the water splitting cells, connected with wires to the immersed catalyst electrodes, and then exposed to simulated solar irradiation that provided the energy to split water. The tandem cell used in the integrated device exhibited the J - V response depicted in Figure 6d, yielding a V_{OC} of 1.7 V while retaining a high PCE of 23.1%. The operating current density of the combined system (normalized to the total illuminated area of the solar cells) is predicted by the intersection of the J - V curves of both the perovskite/Si tandem solar cell and the catalyst electrodes in the two-electrode configuration (Figure 6d). At actual measurement, the PV-EC combined system giving a same current value of the predicted current at figure 6d, 14.24 mA cm^{-2} , indicating our PV-EC system was successfully operated under the standard AM 1.5G insolation conditions. Taking $\eta_F = 100\%$ and $J_{\text{sc}} = 14.24 \text{ mA cm}^{-2}$ (Figure 6e), the STH efficiency was calculated to be 17.52%. The fluctuation of the current under illumination is caused by bubble formation on the surface, which affects the active area. Furthermore, in the current study, the solar cells are wired with the water splitting electrodes; however, alternative architectures are possible. For example, one

can directly attach water splitting catalysts onto the back sides of solar cells to form an integrated system. Compared with other recently reported PV-EC systems, our system is comparable to state-of-the-art solar water splitting systems in terms of the solar-to-hydrogen efficiency (STH) and the solar-to-hydrogen efficiency per photocurrent-to-charge efficiency (STH/PCE) (Table 3-1)^{31, 43-45}

Table 3-1 Comparison between our results and various PV-EC systems that have been reported elsewhere.

Solar cell	2 electrode			Active area (cm^2)		Reference
	overpotential (10 mA cm^{-2})	PCE (%)	STH (%)	Solar cell	Electrocatalyst Ratio	
Perovskite	470 mV	15.7	12.3	0.318	5> ^{a)}	15.7 32
Silicon	-	16.1	7.9	5	1	0.2 41
Silicon	-	12.3	7.5	6.03	9	1.49 42
InGaP/GaAs tandem	-	15.7	10.5	0.031	1	32 43
CIGS/CdS tandem	-	17	10.5	-	4	- 44
Perovskite/Silicon tandem	390 mV	23.1	17.52	0.1875	2	10.6 This Work

^{a)} Ni foam substrate has more immane actual surface area than the projection area.

3-4. Conclusion

In this study, we report a low-cost, highly efficient PV-EC system using earth-abundant electrocatalysts and perovskite/Si tandem solar cells with a promising solar-to-hydrogen efficiency. NiFe (oxy)hydroxide films and Ni₄Mo films show superior water splitting properties than most previously reported electrocatalysts due to the surface morphology and chemical-state control. Combining with the perovskite/Si tandem solar cells, we achieved 17.52% solar-to-hydrogen efficiency, highly efficient than as reported many researches. Our results provide rational design of efficient overall water splitting and push the frontier of PV-EC system. Thus, we expect further improvement of the PV-EC performance via enhancement of the solar cells stability or using alternative cell connecting systems.

3-5. References

- [1] Joya, K. S.; Joya, Y. F.; Ocakoglu, K.; van de Krol, R., Water-splitting catalysis and solar fuel devices: artificial leaves on the move. *Angew Chem Int Ed Engl* 2013, 52 (40), 10426-37.
- [2] Chu, S.; Majumdar, A., Opportunities and challenges for a sustainable energy future. *Nature* 2012, 488 (7411), 294-303.
- [3] Lee, M. G.; Kim, D. H.; Sohn, W.; Moon, C. W.; Park, H.; Lee, S.; Jang, H. W., Conformally coated BiVO₄ nanodots on porosity-controlled WO₃ nanorods as highly efficient type II heterojunction photoanodes for water oxidation. *Nano Energy* 2016, 28, 250-260.
- [4] Lee, M. G.; Moon, C. W.; Park, H.; Sohn, W.; Kang, S. B.; Lee, S.; Choi, K. J.; Jang, H. W., Dominance of Plasmonic Resonant Energy Transfer over Direct Electron Transfer in Substantially Enhanced Water Oxidation Activity of BiVO₄ by Shape-Controlled Au Nanoparticles. *Small* 2017, 13 (37).
- [5] Chang Kwon, K.; Choi, S.; Lee, J.; Hong, K.; Sohn, W.; Andoshe, D. M.; Choi, K. S.; Kim, Y.; Han, S.; Kim, S. Y.; Jang, H. W., Drastically enhanced hydrogen evolution activity by 2D to 3D structural transition in anion-engineered molybdenum disulfide thin films for efficient Si-based water

splitting photocathodes. Journal of Materials Chemistry A 2017, 5 (30), 15534-15542.

[6] Kwon, K. C.; Choi, S.; Hong, K.; Moon, C. W.; Shim, Y.-S.; Kim, D. H.; Kim, T.; Sohn, W.; Jeon, J.-M.; Lee, C.-H.; Nam, K. T.; Han, S.; Kim, S. Y.; Jang, H. W., Wafer-scale transferable molybdenum disulfide thin-film catalysts for photoelectrochemical hydrogen production. Energy & Environmental Science 2016, 9 (7), 2240-2248.

[7] McGlade, C.; Ekins, P., The geographical distribution of fossil fuels unused when limiting global warming to 2 degrees C. Nature 2015, 517 (7533), 187-90.

[8] Benck, J. D.; Hellstern, T. R.; Kibsgaard, J.; Chakthranont, P.; Jaramillo, T. F., Catalyzing the Hydrogen Evolution Reaction (HER) with Molybdenum Sulfide Nanomaterials. ACS Catalysis 2014, 4 (11), 3957-3971.

[9] Osterloh, F. E.; Parkinson, B. A., Recent developments in solar water-splitting photocatalysis. MRS Bulletin 2011, 36 (01), 17-22.

[10] Tachibana, Y.; Vayssières, L.; Durrant, J. R., Artificial photosynthesis for solar water-splitting. Nature Photonics 2012, 6 (8), 511-518.

[11] Liu, R.; Zheng, Z.; Spurgeon, J.; Yang, X., Enhanced photoelectrochemical water-splitting performance of semiconductors by

- surface passivation layers. *Energy Environ. Sci.* 2014, 7 (8), 2504-2517.
- [12] Moniz, S. J. A.; Shevlin, S. A.; Martin, D. J.; Guo, Z.-X.; Tang, J., Visible-light driven heterojunction photocatalysts for water splitting – a critical review. *Energy & Environmental Science* 2015, 8 (3), 731-759.
- [13] Kargar, A.; Sun, K.; Jing, Y.; Choi, C.; Jeong, H.; Zhou, Y.; Madsen, K.; Naughton, P.; Jin, S.; Jung, G. Y.; Wang, D., Tailoring n-ZnO/p-Si branched nanowire heterostructures for selective photoelectrochemical water oxidation or reduction. *Nano Lett* 2013, 13 (7), 3017-22.
- [14] Chen, S.; Wang, L.-W., Thermodynamic Oxidation and Reduction Potentials of Photocatalytic Semiconductors in Aqueous Solution. *Chemistry of Materials* 2012, 24 (18), 3659-3666.
- [15] Landon, J.; Demeter, E.; İnoğlu, N.; Keturakis, C.; Wachs, I. E.; Vasić, R.; Frenkel, A. I.; Kitchin, J. R., Spectroscopic Characterization of Mixed Fe–Ni Oxide Electrocatalysts for the Oxygen Evolution Reaction in Alkaline Electrolytes. *ACS Catalysis* 2012, 2 (8), 1793-1801.
- [16] Nurlaela, E.; Shinagawa, T.; Qureshi, M.; Dhawale, D. S.; Takanabe, K., Temperature Dependence of Electrocatalytic and Photocatalytic Oxygen Evolution Reaction Rates Using NiFe Oxide. *ACS Catalysis* 2016, 6 (3), 1713-1722.
- [17] Wang, M.; Wang, Z.; Yu, X.; Guo, Z., Facile one-step electrodeposition

preparation of porous NiMo film as electrocatalyst for hydrogen evolution reaction. International Journal of Hydrogen Energy 2015, 40 (5), 2173-2181.

[18] Wang, T.; Guo, Y.; Zhou, Z.; Chang, X.; Zheng, J.; Li, X., Ni-Mo Nanocatalysts on N-Doped Graphite Nanotubes for Highly Efficient Electrochemical Hydrogen Evolution in Acid. ACS Nano 2016, 10 (11), 10397-10403.

[19] Wang, X.; Kolen'ko, Y. V.; Bao, X. Q.; Kovnir, K.; Liu, L., One-Step Synthesis of Self-Supported Nickel Phosphide Nanosheet Array Cathodes for Efficient Electrocatalytic Hydrogen Generation. Angew Chem Int Ed Engl 2015, 54 (28), 8188-92.

[20] Popczun, E. J.; McKone, J. R.; Read, C. G.; Biacchi, A. J.; Wiltrot, A. M.; Lewis, N. S.; Schaak, R. E., Nanostructured nickel phosphide as an electrocatalyst for the hydrogen evolution reaction. J Am Chem Soc 2013, 135 (25), 9267-70.

[21] Gong, M.; Li, Y.; Wang, H.; Liang, Y.; Wu, J. Z.; Zhou, J.; Wang, J.; Regier, T.; Wei, F.; Dai, H., An advanced Ni-Fe layered double hydroxide electrocatalyst for water oxidation. J Am Chem Soc 2013, 135 (23), 8452-5.

[22] Lu, Z.; Xu, W.; Zhu, W.; Yang, Q.; Lei, X.; Liu, J.; Li, Y.; Sun, X.; Duan, X., Three-dimensional NiFe layered double hydroxide film for high-efficiency oxygen evolution reaction. Chem Commun (Camb) 2014, 50 (49),

6479-82.

- [23] Hunter, B. M.; Hieringer, W.; Winkler, J. R.; Gray, H. B.; Müller, A. M., Effect of interlayer anions on [NiFe]-LDH nanosheet water oxidation activity. *Energy & Environmental Science* 2016, 9 (5), 1734-1743.
- [24] Chen, W. F.; Sasaki, K.; Ma, C.; Frenkel, A. I.; Marinkovic, N.; Muckerman, J. T.; Zhu, Y.; Adzic, R. R., Hydrogen-evolution catalysts based on non-noble metal nickel-molybdenum nitride nanosheets. *Angew Chem Int Ed Engl* 2012, 51 (25), 6131-5.
- [25] Wang, Y.; Zhang, G.; Xu, W.; Wan, P.; Lu, Z.; Li, Y.; Sun, X., A 3D Nanoporous Ni-Mo Electrocatalyst with Negligible Overpotential for Alkaline Hydrogen Evolution. *ChemElectroChem* 2014, 1 (7), 1138-1144.
- [26] Solmaz, R.; Kardaş, G., Electrochemical deposition and characterization of NiFe coatings as electrocatalytic materials for alkaline water electrolysis. *Electrochimica Acta* 2009, 54 (14), 3726-3734.
- [27] Trotochaud, L.; Young, S. L.; Ranney, J. K.; Boettcher, S. W., Nickel-iron oxyhydroxide oxygen-evolution electrocatalysts: the role of intentional and incidental iron incorporation. *J Am Chem Soc* 2014, 136 (18), 6744-53.
- [28] Trotochaud, L.; Ranney, J. K.; Williams, K. N.; Boettcher, S. W., Solution-cast metal oxide thin film electrocatalysts for oxygen evolution. *J Am Chem Soc* 2012, 134 (41), 17253-61.

- [29] Louie, M. W.; Bell, A. T., An investigation of thin-film Ni-Fe oxide catalysts for the electrochemical evolution of oxygen. *J Am Chem Soc* 2013, 135 (33), 12329-37.
- [30] Friebel, D.; Louie, M. W.; Bajdich, M.; Sanwald, K. E.; Cai, Y.; Wise, A. M.; Cheng, M. J.; Sokaras, D.; Weng, T. C.; Alonso-Mori, R.; Davis, R. C.; Bargar, J. R.; Norskov, J. K.; Nilsson, A.; Bell, A. T., Identification of highly active Fe sites in (Ni,Fe)OOH for electrocatalytic water splitting. *J Am Chem Soc* 2015, 137 (3), 1305-13.
- [31] Luo, J.; Im, J. H.; Mayer, M. T.; Schreier, M.; Nazeeruddin, M. K.; Park, N. G.; Tilley, S. D.; Fan, H. J.; Gratzel, M., Water photolysis at 12.3% efficiency via perovskite photovoltaics and Earth-abundant catalysts. *Science* 2014, 345 (6204), 1593-6.
- [32] Tian, J.; Cheng, N.; Liu, Q.; Sun, X.; He, Y.; Asiri, A. M., Self-supported NiMo hollow nanorod array: an efficient 3D bifunctional catalytic electrode for overall water splitting. *Journal of Materials Chemistry A* 2015, 3 (40), 20056-20059.
- [33] Ci, S.; Mao, S.; Hou, Y.; Cui, S.; Kim, H.; Ren, R.; Wen, Z.; Chen, J., Rational design of mesoporous NiFe-alloy-based hybrids for oxygen conversion electrocatalysis. *Journal of Materials Chemistry A* 2015, 3 (15), 7986-7993.

- [34] Marchetti, L.; Miserque, F.; Perrin, S.; Pijolat, M., XPS study of Ni-base alloys oxide films formed in primary conditions of pressurized water reactor. *Surface and Interface Analysis* 2015, 47 (5), 632-642.
- [35] Feng, Y.; Yu, X. Y.; Paik, U., N-doped graphene layers encapsulated NiFe alloy nanoparticles derived from MOFs with superior electrochemical performance for oxygen evolution reaction. *Sci Rep* 2016, 6, 34004.
- [36] Biesinger, M. C.; Payne, B. P.; Grosvenor, A. P.; Lau, L. W. M.; Gerson, A. R.; Smart, R. S. C., Resolving surface chemical states in XPS analysis of first row transition metals, oxides and hydroxides: Cr, Mn, Fe, Co and Ni. *Applied Surface Science* 2011, 257 (7), 2717-2730.
- [38] Chemelewski, W. D.; Lee, H. C.; Lin, J. F.; Bard, A. J.; Mullins, C. B., Amorphous FeOOH oxygen evolution reaction catalyst for photoelectrochemical water splitting. *J Am Chem Soc* 2014, 136 (7), 2843-50.
- [39] Ali-Löytty, H.; Louie, M. W.; Singh, M. R.; Li, L.; Sanchez Casalongue, H. G.; Ogasawara, H.; Crumlin, E. J.; Liu, Z.; Bell, A. T.; Nilsson, A.; Friebel, D., Ambient-Pressure XPS Study of a Ni–Fe Electrocatalyst for the Oxygen Evolution Reaction. *The Journal of Physical Chemistry C* 2016, 120 (4), 2247-2253.
- [40] Juodkazis, K.; Juodkazytė, J.; Vilkauskaitė, R.; Jasulaitienė, V., Nickel

surface anodic oxidation and electrocatalysis of oxygen evolution. *Journal of Solid State Electrochemistry* 2008, 12 (11), 1469-1479.

[41] Ahlawat, A.; Sathe, V. G.; Reddy, V. R.; Gupta, A., Mossbauer, Raman and X-ray diffraction studies of superparamagnetic NiFe₂O₄ nanoparticles prepared by sol-gel auto-combustion method. *Journal of Magnetism and Magnetic Materials* 2011, 323 (15), 2049-2054.

[42] Iliev, M. N.; Mazumdar, D.; Ma, J. X.; Gupta, A.; Rigato, F.; Fontcuberta, J., Monitoring B-site ordering and strain relaxation in NiFe₂O₄ epitaxial films by polarized Raman spectroscopy. *Physical Review B* 2011, 83 (1).

[43] Schüttauf, J.-W.; Modestino, M. A.; Chinello, E.; Lambelet, D.; Delfino, A.; Dominé, D.; Faes, A.; Despeisse, M.; Bailat, J.; Psaltis, D.; Moser, C.; Ballif, C., Solar-to-Hydrogen Production at 14.2% Efficiency with Silicon Photovoltaics and Earth-Abundant Electrocatalysts. *Journal of The Electrochemical Society* 2016, 163 (10), F1177-F1181.

[44] Verlage, E.; Hu, S.; Liu, R.; Jones, R. J. R.; Sun, K.; Xiang, C.; Lewis, N. S.; Atwater, H. A., A monolithically integrated, intrinsically safe, 10% efficient, solar-driven water-splitting system based on active, stable earth-abundant electrocatalysts in conjunction with tandem III-V light absorbers protected by amorphous TiO₂ films. *Energy & Environmental Science* 2015,

8 (11), 3166-3172.

[45] Jacobsson, T. J.; Fjällström, V.; Sahlberg, M.; Edoff, M.; Edvinsson, T., A monolithic device for solar water splitting based on series interconnected thin film absorbers reaching over 10% solar-to-hydrogen efficiency. *Energy & Environmental Science* 2013, 6 (12).

[46] Li, J.; Wang, Y.; Zhou, T.; Zhang, H.; Sun, X.; Tang, J.; Zhang, L.; Al-Enizi, A. M.; Yang, Z.; Zheng, G., Nanoparticle Superlattices as Efficient Bifunctional Electrocatalysts for Water Splitting. *J Am Chem Soc* 2015, 137 (45), 14305-12.

[47] Park, I. J.; Park, J. H.; Ji, S. G.; Park, M.-A.; Jang, J. H.; Kim, J. Y., A Three-Terminal Monolithic Perovskite/Si Tandem Solar Cell Characterization Platform. *Joule* 2018.

Chapter 4 Novel and promising electrocatalyst for oxygen evolution reaction based on medium entropy alloy

4-1. Introduction

In our previous work, I introduced Ni-based electrocatalysts with nanostructured surface and nanometer scale grain size to overcome the current limitation of transition metal based electrocatalysts, as mentioned in Chapter 2. I achieved the highly efficient electrocatalysts in terms of overpotential to achieve current density of 10 mA/cm^2 (270 mV) and tafel slope (44.4 mV). Despite the substantial improvement of water splitting activity of transition metal based anodes, it is still low to replace the noble metal based catalysts or fossil fuels. Therefore, another approach is needed to overcome these drawbacks and reach a practical solution of this issue like explore the new metal alloy compositions.

4-1-1. High entropy alloy and Medium entropy alloy

High entropy alloys (HEAs) and medium entropy alloys (MEAs) has attracted increasing attention due to the extreme stability in the harsh environment, especially at strong acid. Simply, high entropy alloys are defined as the alloys with configuration entropy is larger than 1.5 R (R is gas constant) and medium entropy alloys are defined as the alloys with configuration entropy between 1 R and 1.5 R. HEAs and MEAs has special electrochemical properties like sluggish diffusion, lattice distortion due to the different size of atoms, and synergistic effect named cocktail effect. The advantages like similar stability and large-variation of composition, MEAs considered more appropriated to the water splitting reaction. In the HEAs, all of the atoms should exist same amount but MEAs could change the ratio to suit the purpose. In this study, as an effort to enhance water splitting activities, we employ new MEAs that favorable to oxygen evolution reaction.

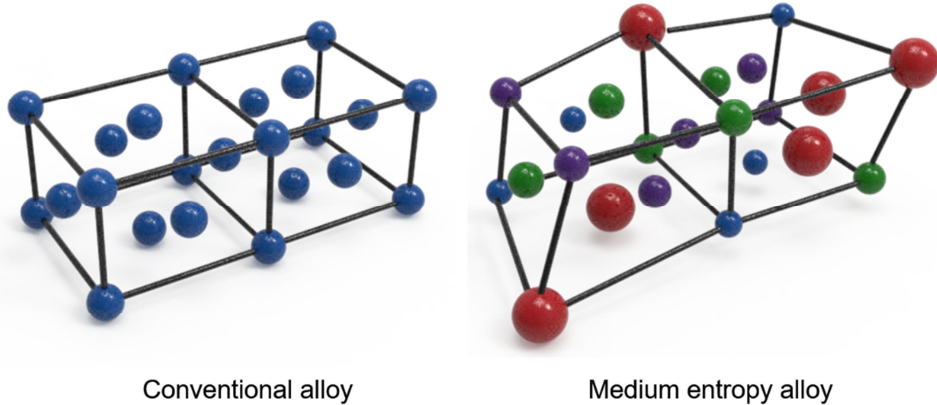


Figure 4-1 Schematic illustration of conventional alloy and medium entropy alloy.

4-2. Experimental method and characterization

4-2-1. Alloy preparation

The ingot with a nominal composition was prepared by vacuum induction melting (MC100V, Indutherm, Walzbachtal-Wossingen) of pure elements (purity greater than 99.9%) under an Argon atmosphere. The as-cast ingot was homogenized at 1200 °C for six hours in an argon atmosphere, followed by water quenching. The homogenized sample was milled to a thickness of \sim 7 mm, and cold rolled to the thickness of 1.5 mm (78% of thickness reduction). The cold-rolled plate was annealed at 800 °C and 1200 °C for 60 min, followed by water quenching.

4-2-2. Microstructure characterization

The scanning electron microscopy (SEM) in back scattered electron mode (BSE) and energy dispersive spectroscopy (EDS) mapping of annealed samples were analyzed using high-resolution field emission scanning electron microscope (HR-FE-SEM-II, JSM 7,800F PRIME with Dual EDS). The electron backscattered diffraction (EBSD) analysis of the annealed and deformed samples was carried out using field-emission scanning electron microscopy (FE-SEM, Helios, Hikari, UMS II). The EBSD data of sample annealed at 800 °C and 1200 °C were acquired by using the step size of 0.22 μm and 1.8 μm, respectively. The EBSD data of deformed sample was acquired by using the step size of 0.12 μm (800 °C annealed and deformed sample) and 1.20 μm (1200 °C annealed and deformed sample). The EBSD data were analyzed by TSL OIM data collection software (TSL OIM Analysis 7). The fraction of B2 and sigma phase were estimated from several low magnification BSE images using ImageJ software (open-source software developed by the National Institute of Health (NIH) of USA). The fraction of recrystallized and non-recrystallized regions are estimated from EBSD-grain orientation spread (GOS) at low magnification from several images [11]. The fractions of recrystallized coarse and fine grains are estimated by grain size partitioning, considering grain size > 10 μm as

coarse grains and excluding non-recrystallized regions. The kernel average misorientation (KAM) map was calculated up to the third neighbor kernel with an average misorientation angle of 5°[25] . Samples for EBSD were mechanically polished by SiC papers followed by diamond and colloidal polishing. TEM samples along the crosssection perpendicular to rolling direction/tensile direction were prepared by focus ion beam (FIB) lift out procedure using Dual Beam FIB (Helios, Hikari, UMS II).

4-2-4. Electrochemical characterization

To analysis PEC properties of the BiVO₄-based photoanodes, I used previously reported measurement, as stated in Chapter 2 and Chapter 3.

4-3. Results and discussion

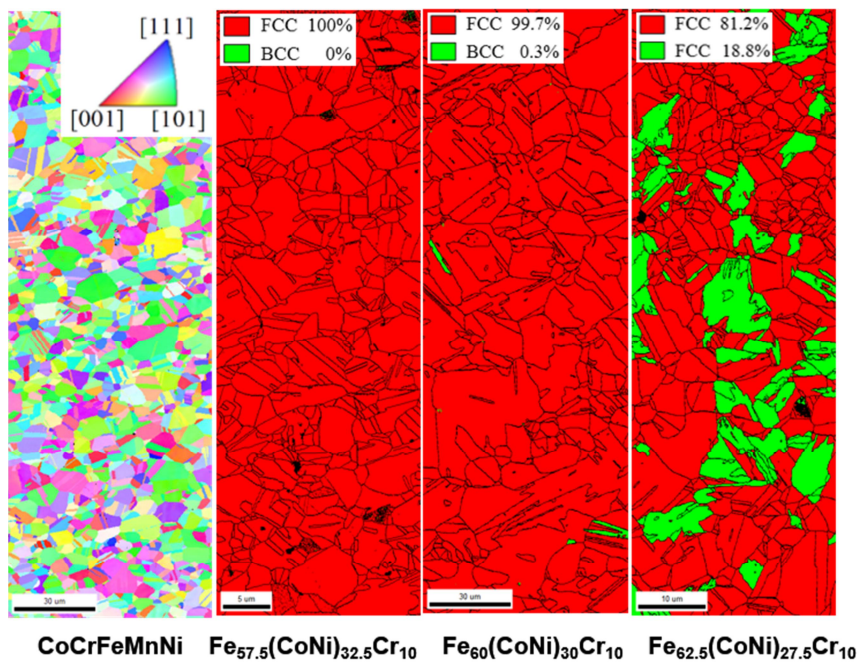


Figure 4-2 EBSD images of fabricated HEA and MEAs.

4-3-1. Fabrication of HEAs and MEAs

Firstly, for the comparison between HEAs and MEAs at water splitting reaction, CoCrFeMnNi and CoCrNi is employed as the reference, the typical composition of HEAs and MEAs. Furthermore as favorable to water splitting reaction, MEAs with Fe-60 atomic percent are evaluated to find efficient electrocatalysts. As shown in figure 4-2 and 4-3, HEAs and MEAs has single FCC phase except MEAs with Fe-62.5 atomic percent.

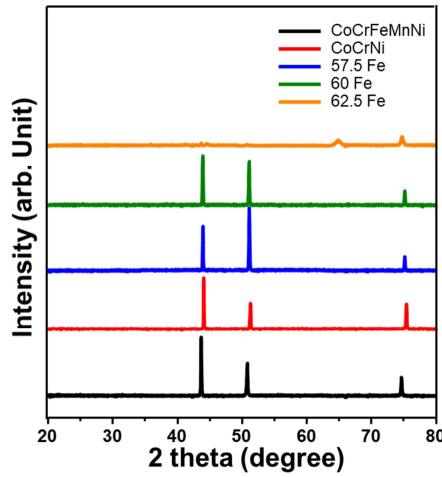


Figure 4-3 X-ray diffraction patterns of HEA and MEAs.

4-3-2. Hydrogen evolution properties of HEAs and MEAs

The water splitting tendency of hydrogen evolution reaction of HEA and MEAs are shown at figure 4-4. Extraordinary properties of MEAs with 62.5 atomic percent Fe is due to the BCC phase, and overall

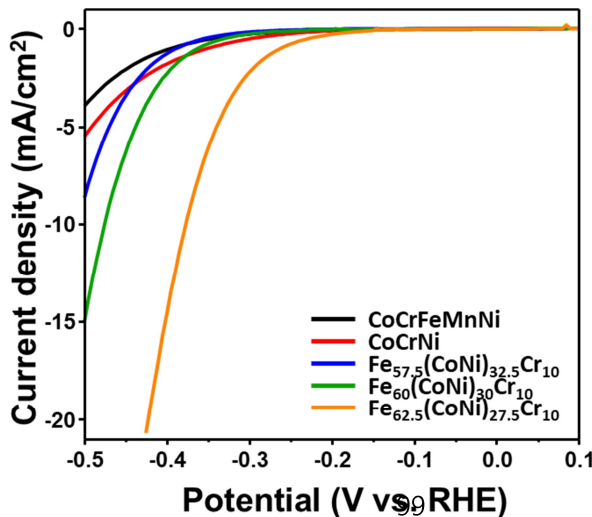


Figure 4-4 Hydrogen evolution reaction of HEA and MEAs.

activities are strongly low than reported many hydrogen evolution catalysts. To overcome bottleneck reaction of water splitting, oxygen evolution reaction, we concentrated on the oxygen evolution catalysts, as shown in figure 4-4.

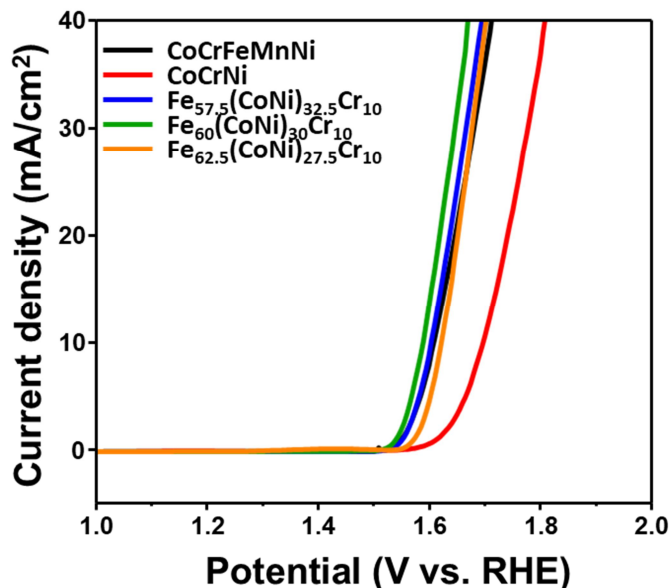


Figure 4-5 Oxygen evolution reaction of HEA and MEAs.

4-3-1. Oxygen evolution properties of HEAs and MEAs

As expected, the oxygen evolution reaction of HEA and MEAs shows different efficiency because of compositional diversity. The lowest properties of CoCrNi is due to the lack of Fe ions, favorable to oxygen evolution reaction, MEAs with 60 atomic percent Fe shows

highest efficient due to the optimal composition of alloys. The overpotential to achieve current density of 10 mA/cm² is 358 mV, greatly lower than conventional NiFe alloy, around 400mV. Based on this results, further process is conducted to enhance the oxygen evolution properties of MEAs.

4-3-4. Oxygen evolution properties of HEAs and MEAs after

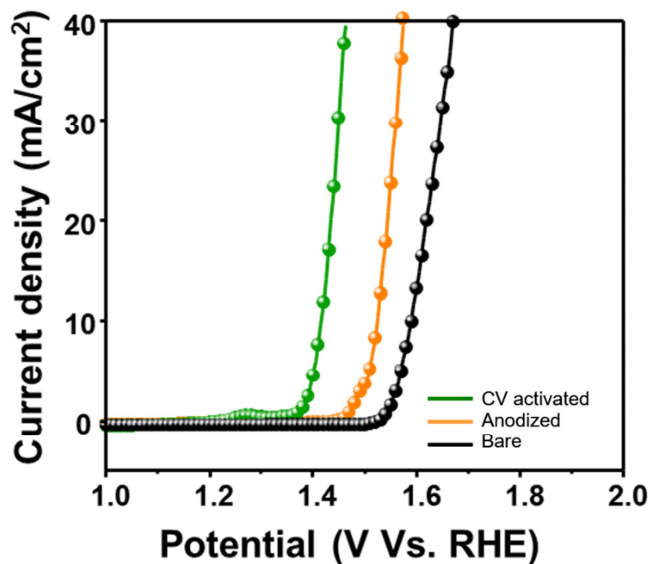


Figure 4-6 Oxygen evolution reaction of Fe₆₀(CoNi)₃₀Cr₁₀ MEAs after anodization and CV activation

As mentioned at Chapter 3, anodization is powerful method to successively synthesize the high efficient metal oxide/hydroxide with porous surface. Same technique is applied to MEAs to increase overall water splitting properties. In addition to anodization, CV activation also conducted to further increase of oxygen evolution properties, for increase the metal oxide/hydroxide and surface purification. As a result of anodization and CV activation, figure 4-3, the overpotential to achieve current density 10 mA/cm^2 is extremely decreased, from 358 to 184 mV. The overpotential of 184 mV is lowest value that reported, in terms of MEAs and solution processed electrocatalysts.

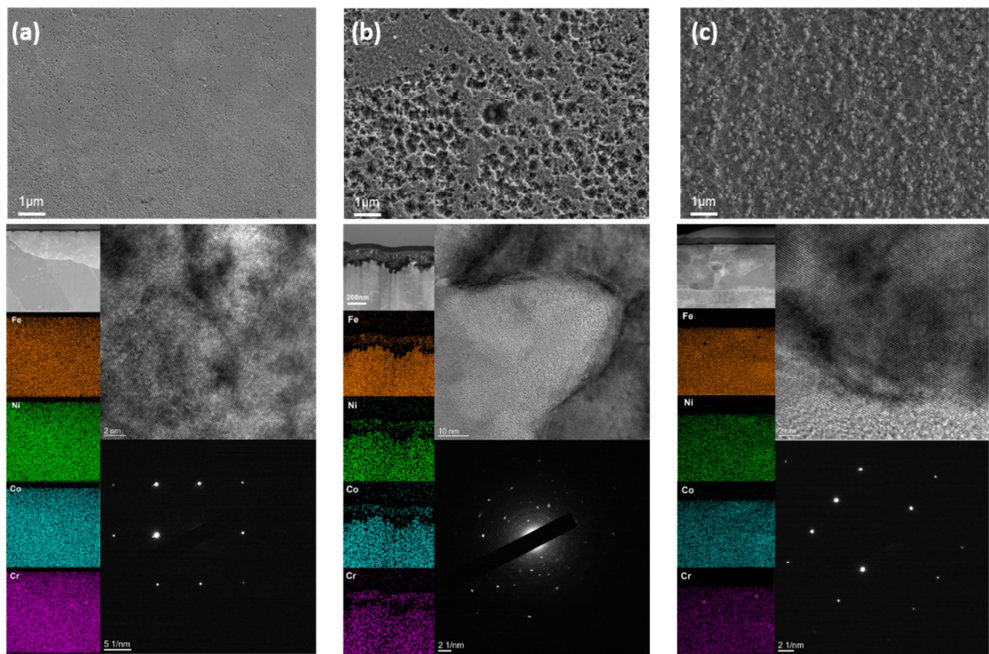


Figure 4-7 SEM and TEM images of (a) Bare $\text{Fe}_{60}(\text{CoNi})_{30}\text{Cr}_{10}$ MEAs, (b) anodized MEAs, and (c) CV activated MEAs after anodization.

4-3-5. Surface characterization of HEA and MEAs

The surface morphology and EDS mapping is conducted after anodization and CV activation, respectively.

Fabricated $\text{Fe}_{60}(\text{CoNi})_{30}\text{Cr}_{10}$ MEAs shows extremely flat surface and cross-section images. After anodization, the surface of $\text{Fe}_{60}(\text{CoNi})_{30}\text{Cr}_{10}$ MEAs has massive micrometer scale pores, exhibiting large surface area. After further catalyst synthesize process,

CV activation, the surface of $\text{Fe}_{60}(\text{CoNi})_{30}\text{Cr}_{10}$ MEAs has protrusion oxide layers, favorable to oxygen evolution reaction.

We expect the further chemical analysis like XPS, Raman and electrochemical analysis such as ECSA measurement could reveal the reason of enhanced oxygen evolution activities.

4-4. Conclusion

I studied the HEA and MEAs as the new candidates for efficient oxygen evolution catalysts to overcome the current limitation and drawbacks of as reported transition metal based electrocatalysts, and found that medium entropy alloy with optimized ratio of Fe, Ni, Co, Cr showed superior electrochemical water splitting properties than any reported solution based electrocatalysts. The anodized metal alloys showed a markedly reduced overpotential to achieve current density of 10 mA/cm^2 assisted by increased active surface area and formation of metal (oxy)hydroxide. Further CV activation process conformally generate the massive protrusion metal (oxy)hydroxide layer on the surface of MEAs, successively increase the overall water splitting properties of MEAs. These findings have recently been employed to guide the design of a new electrocatalysts based on transition metal based alloys. These results shed light on the clue that more

optimal composition for electrocatalysts is existed, over 4 or more atoms, give a critical adjustable parameter in the optimization of the water splitting system. We expect the extensive analysis like XPS or ECSA could clearly reveal the reasons of enhanced water splitting properties, in terms of synergistic effect, anodization, and CV activation.

4-5. References

- [1] Sathiyamoorthi, P.; Park, J. M.; Moon, J.; Bae, J. W.; Asghari-Rad, P.; Zargaran, A.; Seop Kim, H., Achieving high strength and high ductility in Al0.3CoCrNi medium-entropy alloy through multi-phase hierarchical microstructure. *Materialia* 2019, 8.
- [2] Kim, J. G.; Bae, J. W.; Park, J. M.; Woo, W.; Harjo, S.; Chin, K. G.; Lee, S.; Kim, H. S., Synergetic strengthening of layered steel sheet investigated using an in situ neutron diffraction tensile test. *Sci Rep* 2019, 9 (1), 6829.
- [3] Jo, Y. H.; Jung, S.; Choi, W. M.; Sohn, S. S.; Kim, H. S.; Lee, B. J.; Kim, N. J.; Lee, S., Cryogenic strength improvement by utilizing room-temperature deformation twinning in a partially recrystallized VCrMnFeCoNi high-entropy alloy. *Nat Commun* 2017, 8, 15719.
- [4] Yang, T.; Zhao, Y. L.; Liu, W. H.; Zhu, J. H.; Kai, J. J.; Liu, C. T., Ductilizing brittle high-entropy alloys via tailoring valence electron concentrations of precipitates by controlled elemental partitioning. *Materials Research Letters* 2018, 6 (10), 600-606.
- [5] Li, Z.; Raabe, D., Strong and Ductile Non-equiaatomic High-Entropy

Alloys: Design, Processing, Microstructure, and Mechanical Properties. *Jom* 2017, 69 (11), 2099-2106.

[6] Zhou, Y.; Zhou, D.; Jin, X.; Zhang, L.; Du, X.; Li, B., Design of non-equiautomic medium-entropy alloys. *Sci Rep* 2018, 8 (1), 1236.

[7] Eißmann, N.; Klöden, B.; Weißgärber, T.; Kieback, B., High-entropy alloy CoCrFeMnNi produced by powder metallurgy. *Powder Metallurgy* 2017, 60 (3), 184-197.

[8] Glasscott, M. W.; Pendergast, A. D.; Goines, S.; Bishop, A. R.; Hoang, A. T.; Renault, C.; Dick, J. E., Electrosynthesis of high-entropy metallic glass nanoparticles for designer, multi-functional electrocatalysis. *Nat Commun* 2019, 10 (1), 2650.

[9] Moravcik, I.; Gouvea, L.; Cupera, J.; Dlouhy, I., Preparation and properties of medium entropy CoCrNi/boride metal matrix composite. *Journal of Alloys and Compounds* 2018, 748, 979-988.

[10] Yusenko, K. V.; Riva, S.; Carvalho, P. A.; Yusenko, M. V.; Arnaboldi, S.; Sukhikh, A. S.; Hanfland, M.; Gromilov, S. A., First hexagonal close packed high-entropy alloy with outstanding stability under extreme conditions and electrocatalytic activity for methanol oxidation. *Scripta Materialia* 2017, 138, 22-27.

- [11] Gludovatz, B.; Hohenwarter, A.; Thurston, K. V.; Bei, H.; Wu, Z.; George, E. P.; Ritchie, R. O., Exceptional damage-tolerance of a medium-entropy alloy CrCoNi at cryogenic temperatures. *Nat Commun* 2016, 7, 10602.
- [12] Zhang, Z.; Sheng, H.; Wang, Z.; Gludovatz, B.; Zhang, Z.; George, E. P.; Yu, Q.; Mao, S. X.; Ritchie, R. O., Dislocation mechanisms and 3D twin architectures generate exceptional strength-ductility-toughness combination in CrCoNi medium-entropy alloy. *Nat Commun* 2017, 8, 14390.

6. Summary

This thesis cover the fundamental working principle, mechanism, diverse analysis method and crucial parameter of electrochemical water splitting and PV-EC system. Various approaches to overcome limitations of conventionally reported transition metal based electrocatalysts like NiFe and NiMo for electrochemical water splitting reaction. The drawbacks of transition metal based electrocatalysts, deficient efficiency to replace noble metal based catalysts and fossil fuels, sluggish oxygen evolving reaction kinetics on anode surface were managed by employing the several engineering strategies such as grain boundary engineering, nanostructuring, anodization, CV activation, and exploring new compositions.

First, control of the surface grain boundary density could increase active surface and change the rate determining step, more favorable to oxygen evolution reaction. The optimized composition and maximized surface grain boundary density NiFe binary alloy electrocatalysts can lead to a low overpotential to achieve current density of 10 mA/cm^2 , just for 300 mV without additional co-catalyst. Second the direct anodization of metal alloys can effectively enhance overall water splitting properties in terms of

increased active surface area and successively formed metal (oxy)hydroxide layer on the surface. The choice of proper precursor and acid electrolytes for anodization condition is a key to maximize the electrochemical water splitting efficiency of metal alloy electrocatalysts. Third, medium entropy alloys and high entropy alloys are evaluated to explore new composition for highly-efficient water splitting catalysts. Combined electrocatalyst fabrication technique, anodization and CV activation extremely enhance the oxygen evolution activities of MEAs. These results are almost sufficient properties to replace noble metal based electrocatalysts or fossil fuels, in terms of overpotential, stability, and economically. In this point of view, this study provides deep insight to design practically usable electrocatalysts for hydrogen production.

Abstract (in Korean)

고효율 촉매전극을 위한 다원계 금속 합금 전기 촉매

연구

전이금속을 기반으로 하는 전기촉매는 귀금속 계열 촉매의 가격적 한계를 극복하기 위하여 연구되어지는 매우 전도 유망한 재료이다. 그러나 기존까지 보고된 전이금속 기반 전기촉매의 물분해 특성은 귀금속 계열 촉매를 대체하기에는 부족한 수준이다.

본 논문에서는 전이금속을 기반으로 한 고효율 전기촉매를 합성하기 위하여 다양한 방법과, 태양전지와 전기촉매의 결합을 통하여 추가적인 전압장치 없이도 수소를 생산할 수 있는 PV-EC 시스템에 대하여 보고하였으며 이를 통해 전이금속을 기반으로 한 전기촉매가 현재의 귀금속 계열 전기촉매보다 충분히 우수한 특성을 가질 수 있으며 따라서 현재의 에너지 위기를 극복할 수

있는 물분해 촉매로서 충분한 잠재력을 가지고 있음을 확인하였다.

이를 위해 크게 세 가지 연구를 진행하였는데, 이는 다음과 같다.

첫 번째 연구에서는 동일한 촉매의 전반적인 물분해 특성을 향상시키기 위하여 표면의 그레인 바운더리 비율을 조절하였다. 먼저 아크-멜팅 기법으로 20 마이크로미터와 440 마이크로미터 크기의 그레인을 가지는 철-니켈 이원계 금속 합금을 만들고 두 합금의 물분해 특성을 평가하였다. 이를 통해 동일한 상태의 전기촉매에서도, 그레인 크기에 따라 물분해 특성이 의미 있는 수준으로 달라진다는 것을 확인하였다. 더 나아가 전기전착법으로 나노미터 크기의 그레인을 가지는 철-니켈 이원계 금속 합금을 만들어 그레인 크기가 더 작아지면 물분해 특성이 추가적으로 향상될 수 있다는 것 역시 확인하였다. 최적 조건 하에서, 철-니켈 이원계 금속 합금은 10 mA/cm^2 의 전류밀도를 얻기 위하여 300 mV 의 과전압이 필요한 수준의 전기 촉매를 합성하였으며 다양한 방법을 통하여 특성 향상의 원인을 분석하였다. 우선 첫째로, 타펠 기울기와 버틀러-볼머 공식을 적용하여 비교해보면 전하전달 단계의 상대적 에너지 장벽 크기가 변화하여 속도결정단계가 S_0 에서 S_1 로 바뀐다는 것을 확인하였다. 둘째로 ECSA 분석법을

활용하여 그레인 바운더리의 농도가 높아짐에 따라 표면의 활성표면적이 늘어난다는 것을 확인하였다. 이러한 분석을 바탕으로 그레인 바운더리는 전기촉매의 전체 반응 경로와 활성 표면적에 직접적으로 영향을 준다는 것을 밝혀내었다. 이는 산소발생반응에서 그레인 바운더리가 어떻게 영향을 주는지에 대해 분석한 첫 번째 결과이며, 이러한 개념은 다양한 광전극 시스템에 적용이 가능하다.

이를 응용하여 두 번째 연구에서는 용액공정으로 합성하여 나노미터 크기의 그레인을 가지는 철-니켈 수산화물의 전기촉매를 합성하고, 이에 따른 물분해 특성 및 기준 보고된 전기촉매와의 차이점을 다양한 관점에서 분석하였다. 롤투롤 방법으로 합성된 철-니켈 이원계 금속 합금에 양극산화법을 도입한 간편한 합성법을 이용하여 높은 안정성 및 고효율 물분해 특성을 얻었으며 이는 크게 다음과 같은 두 가지로 분석해 볼 수 있다. 1. 양극산화 공정은 금속의 표면을 산화시켜 다공성 산화막을 형성하는 방법으로, 물분해 반응에 유리한 철-니켈 수산화막을 극대화된 표면적을 가지도록 표면에 고르게 형성할 수 있다. 2. 양극산화 공정 전후의 표면 화학 분석을 비교해보면, 양극산화 후

처음에 비해 니켈과 철의 3가 이온의 존재가 눈에 띄게 증가하는데, 이를 통해 금속 수산화물(M-OH) 보다 우수한 물분해 특성을 같은 M-OOH 가 형성된다는 것을 알 수 있다. 기존의 용액공정을 이용한 철-니켈 기반 전기촉매 합성 방법은 크게 전기전착법과 수열합성법이 있는데, 본 연구에서 사용한 양극산화법은 전기전착법과 비교하여 M-OOH 의 비율이 늘어나고 효율 전기촉매를 기대할 수 있으며, 수열합성법보다 저온과 짧은 반응시간으로 간편하게 전기촉매를 합성할 수 있어 경제적으로도 우수한 방법이다. 또한 대면적 합성이 가능하여 실제 산업에도 충분히 적용이 가능할 것으로 기대된다. 더 나아가 페로브스카이트/실리콘 태양전지와 연결하여 17.5 퍼센트의 solar-to-hydrogen (STH) 효율을 얻었으며, 이는 기존 보고된 1 sun 조건에서의 PV-EC 시스템 중 가장 우수한 결과를 나타낸다. 이를 통해 전이금속을 기반으로 한 전기촉매를 활용한 물분해를 통하여 현재 사용되고 있는 화석연료 기반 수소생산방식을 대체할 수 있을 것으로 기대된다.

세 번째는 연구에서는 중간 엔트로피 합금 (MEAs)을 이용한 새로운 전기촉매 물질을 탐색하였다. 하이 엔트로피 합금 (HEAs)와

중간 엔트로피 금속 합금 (MEAs)은 강산과 같은 극한의 환경에서 도 높은 안정성을 특징으로 가지고 있기 때문에 최근 각광받고 있는 물질이다. 여러 가지 금속이 합금을 이루게 되면, 각각의 원소들 사이의 상승 효과에 의해 다양한 특성을 띄게 되는데 이를 이용하여 MEA의 조성을 잘 이용하면 고효율 물분해 촉매 물질을 찾을 수 있을 것으로 기대된다. 특히 MEA의 경우 HEA 보다 조성의 선택권이 넓어 물분해에 유리한 철과 같은 물질의 비율을 높일 수 있으며, 본 연구에서는 이를 이용하여 가장 높은 효율의 물분해 특성을 가진다고 알려진 철-60% 함유된 합금을 중심으로 MEA의 특성을 비교하였다. 금속 합금에 각각 양극산화법과 CV 활성화법을 적용한 결과, 전류밀도 10 mA/cm^2 를 얻기 위한 과전압이 184 mV로 기존에 보고되는 전기촉매에 비하여 월등히 우수한 결과를 보였다. 이는 금속 합금의 조성과 표면적 및 표면의 화학적 상태를 산소발생반응이 빠르게 일어날 수 형태로 변화시켰기 때문에 가능하였다. 본 연구를 통해 효과적인 산소발생반응을 위한 새로운 재료 후보군을 탐색하였으며, 다양한 금속 원소 간의 상승 효과에 의한 것임을 밝혀내었다.

본 논문에서는 위 연구들을 통해 전이금속 기반의 전기촉매를 활용하여 물분해 특성을 효과적으로 증진시킬 수 있음을 보였으며 기존의 한계를 극복할 수 있는 새로운 물질을 탐색하였다. 또한, 본 연구를 통해 밝혀진 결과들은 다양한 금속 합금 및 금속 수산화물 물분해 촉매에 적용이 가능하며, 물분해 시스템 개발, 수소 생산 및 효율 극대화를 위한 새로운 접근법을 제시하는 바이다.

키워드: 금속 수산화물, 전기화학적 물분해, 철-니켈 합금, 중간 엔트로피 합금 (MEAs), 나노구조, 전기 촉매, 전기전착

학번: 2013-22476

성명: 박 훈 기